Development of a Microfluidic Device for Blood Oxygenation by Photocatalysis
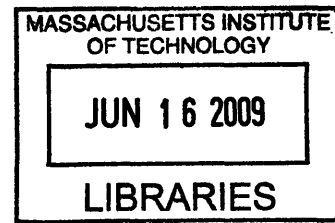
by

Tania Ullah

S.B. Mechanical Engineering
Massachusetts Institute of Technology, 2007

SUBMITTED TO THE DEPARTMENT OF MECHANICAL ENGINEERING IN
PARTIAL FULFILLMENT OF THE REQUIREMENTS FOR THE DEGREE OF

MASTER OF SCIENCE IN MECHANICAL ENGINEERING
AT THE
MASSACHUSETTS INSTITUTE OF TECHNOLOGY

JUNE 2009

© 2009 Massachusetts Institute of Technology.
All rights reserved

Signature of Author: _____

Department of Mechanical Engineering
May 8, 2009

Certified by: _____

Todd Thorsen
Associate Professor of Mechanical Engineering
Thesis Supervisor

Certified by: _____

Richard Gilbert
Visiting Scientist, Department of Mechanical Engineering
Thesis Supervisor

Accepted by: _____

David Hardt
Graduate Officer, Department of Mechanical Engineering

(This page intentionally left blank)

Development of a Microfluidic Device for Blood Oxygenation by Photocatalysis

by

Tania Ullah

Submitted to the Department of Mechanical Engineering on May 8, 2009 in Partial Fulfillment of the Requirements for the Degree of Master of Science in Mechanical Engineering

Abstract

Recent statistics provided by the American Lung Association assert that over 400,000 Americans die every year from lung disorders and more than 35 million are now living with symptoms of lung disease. Mortality rates of heart disease and certain cancers have declined in recent years partly due to improvements in diagnostic testing and the development of targeted medical technologies. Such improvements have not translated over to the treatment of lung disease and lung cancer. The goal of the artificial respiration project is to create a self-contained, mobile oxygen supply that is suitable for implantation and that can potentially replace acute or chronically disabled lungs.

A novel microfluidic device for the oxygenation of whole blood has been developed. The device couples a semiconductor, titanium dioxide (TiO_2), thin film that generates oxygen through photocatalysis with a microfluidic network that facilitates diffusion of the dissolved oxygen to red blood cells. While true pulmonary respiration relies on passive diffusion of oxygen gas from the environment to the blood, the proposed device differs in that it generates oxygen directly from the water in blood plasma. This thesis focuses on the work done to fabricate and characterize the semiconductor photocatalyst, design the integrated microfluidic chip, and validate its capacity to oxygenate blood in real-time.

Blood oxygenation experiments show that the microfluidic device exhibiting the best performance produced 4.06 mL of oxygen per 100 mL of blood, nearly two-thirds of the oxygen transferred in the lung. The flux of oxygen at the photocatalyst surface was 1.11×10^{-3} mmol O_2/ ($cm^2 \cdot$ min). The O_2 flux is nearly two orders of magnitude larger than that of any other fluidic device for blood oxygenation to date. The results from the proof-of-concept microfluidic device are promising and are a step towards the realization of a photocatalytic artificial lung.

Thesis supervisor: Todd Thorsen
Title: Associate Professor of Mechanical Engineering

(This page intentionally left blank)

Acknowledgements

There are many friends and colleagues I would like to thank for helping me throughout my years here at MIT. The Institute has exposed me to the most productive, brilliant, inspiring, creative and fun-loving individuals I know, and for that I am very grateful.

I would first like to thank my thesis advisors, Todd Thorsen and Richard Gilbert, for their invaluable support as I explored the many directions in which this project took me and attempted to find my niche in a field entirely new to me. I am especially appreciative of the patience you two exhibited as I encountered the inevitable stumbling blocks of experimental research.

I also extend my thanks to the other members of the Thorsen Group. Marco Rasponi, you were instrumental in defining the direction the artificial respiration project would take and taught me a great deal about how to conduct quality research. Chien Chih Huang and Raymond Lam, you two were great sources of information and help when I felt as though I was really stuck with my work. Sumeet Kumar, thanks for your friendship and advice, and the fun times we had in the lab.

I cannot forget to thank the members of Professor Caroline Ross's group who answered all my questions about metal oxide film deposition, Kurt Broderick of the Microsystems Technology Laboratories staff who became my fab guru, and the countless other brains I have picked over the last two years. It is amazing how much one can learn from one's colleagues.

Last, but certainly not least, I would like to thank my dear parents and siblings who have supported me throughout my journey at MIT. I really could not have done this without you!

(This page intentionally left blank)

Contents

List of Tables and Figures

Chapter 1

Introduction

Every year, almost 400,000 Americans die from lung disease, and it is the number three killer in the country (behind heart disease and cancer), responsible for 1 in 6 deaths.[1] The lung disease death rate has been increasing over the last decade, while death rates due to other leading causes of death have been declining. Asthma and chronic obstructive pulmonary disorder (COPD) are the most common obstructive lung diseases, with more than 12 million people currently diagnosed with COPD and another 12 million who likely have the disease without knowing it.[2] Additionally, the National Heart Lung and Blood Institute estimates that about 190,000 Americans are affected annually by acute respiratory distress syndrome (ARDS) – a life-threatening condition in which normal gas exchange is compromised by severe buildup of fluid in both lungs.[1] Furthermore, lung disease and various forms of respiratory problems constitute one leading cause of death of babies under the age of one. These disheartening statistics, as well as the fact that lung disease costs the US economy approximately $154 billion in direct and in-direct health-care expenditures,[1] provides us the incentive to develop solutions to address chronic and acute respiratory illnesses.
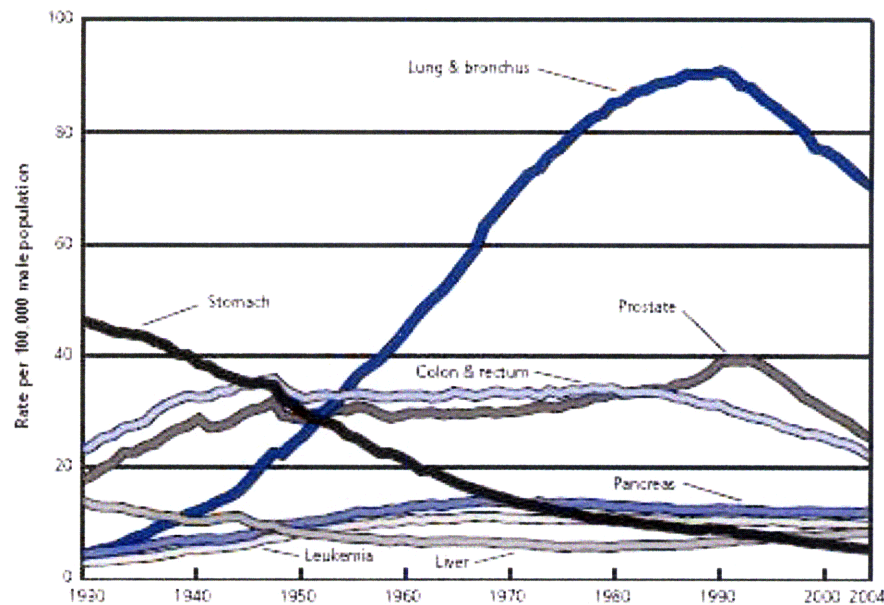
Figure 1.1: Age-adjusted Cancer Death Rates for Males in the US, 1930-2004. This graph, reproduced from the American Cancer Society 2008 Cancer Facts & Figures Report, shows that cancer of the lung and bronchus remains one of the leading causes of cancer death.

Mortality rates of heart disease and certain cancers have declined in recent years partly due to improvements in diagnostic testing and the development of targeted medical technologies. Such improvements have not translated over to the treatment of lung disease and lung cancer. Current treatments include medication (e.g. corticosteroids to reduce inflammation in the airways and antibiotics to treat bacterial infections), mechanical ventilation (e.g. negative and positive pressure devices that increase the amount of air moving into the lungs), oxygen therapy (e.g. extracorporeal membrane oxygenation (ECMO)), and surgery (e.g. lung transplantation and lung reduction surgery to excise diseased tissue). Non-surgical treatments, although they provide brief respite from the symptoms of respiratory disease, are not sufficient standards of care for chronic sufferers. For example, in ECMO, a treatment technique in which cannulae are inserted into the large vessels in the body and blood is pumped through gas-permeable membranes in order to facilitate oxygen and carbon dioxide exchange, there is a significant risk to the patient of thrombosis (blood clotting), infection, and bleeding under anticoagulant medication.[3] Other downsides to ECMO, which has been used consistently

since the early 1970s, include the requirement of a large pumping power to flow the blood through the machine, biofouling on the machine's membranes due to protein and platelet adhesion, and high cost of operation.[4]

Select patients with end-stage lung disease, for whom conventional therapies will not improve life expectancy or alleviate symptoms, lung transplantation remains the only option. However, according to the Scientific Registry of Transplant Recipients, 14% of those on the national waitlist between 2007 and 2008 died before they could receive a lung. For those who received a graft, the survival rate 3 years after implantation plummeted by 30%.[5] Even in the case where lung transplant is successful, patients must take autoimmune drugs for the rest of their life.[6] The transplanted lung is "foreign" to the body and, as a result, there is the possibility of rejection. Patients who receive new lungs must take the autoimmune drugs to suppress the body's natural rejection process.

1.1 Overview of the microfluidic device for photocatalytic blood oxygenation

This thesis discusses a novel approach to developing a device to oxygenate blood – an "artificial lung". As discussed earlier, current treatments for lung disease are not completely effective, nor are they sustainable in the long term. The goal of the artificial respiration project is to create a self-contained, mobile oxygen supply that is suitable for implantation and that can potentially replace acute or chronically disabled lungs. The device that is presented in this thesis has the potential of sustaining human respiration because no refillable tank of gas or pumping power is involved. The oxygenation of the blood works on the following principle: oxygen is generated in the fluid stream directly from the dissociation of water in the blood plasma.

The device couples a semiconductor titanium dioxide (TiO_2) thin film that generates oxygen through photocatalysis with a microfluidic network that facilitates diffusion of the dissolved oxygen to red blood cells. When the thin film semiconductor is irradiated with ultraviolet (UV) light (of wavelength $\lambda = 365$ nm), electron vacancies, or holes, are

generated and migrate toward the surface to provide sites for oxidation. Blood flowing in the PDMS microchannel is in direct contact with the TiO_2 photocatalyst and the water present in blood is oxidized to aqueous oxygen, ready to bind to red blood cell hemoglobin. In this manner, the proposed implantable device will be capable of saturating flowing blood with oxygen in *real-time*. Real-time oxygenation means that with one pass through the device, blood can go from venous levels of oxygen saturation to arterial levels.

As this is a project that resides at the intersection of multiple disciplines, research in artificial respiration technology can lead in several directions. The breakdown of the areas in which we are looking to make developments are as follows:

1) *Optimizing the function of the thin film semiconductor photocatalyst*

The generation of oxygen from photocatalytic water dissociation needs to be sufficient in order to sustain cellular respiration in the tissues of the body. Our goal is to maximize the oxidative potential of the photocatalyst by optimizing thin film processing.

2) *Microfluidic channel scaling and geometry to improve mass transport*

Previous studies have investigated microcapillary branching in channels molded in polydimethylsiloxane (PDMS), mimicking the architecture of pulmonary capillaries. The blood flow in these designs, however, is limited due to high rates of hemolysis and intraluminal clotting.[4,7]

3) *Optics module to efficiently deliver UV light to semiconductor*

The semiconductor is activated by light in a narrow band within the UV range (with a peak activation at $\lambda = 365$ nm) and there is a maximum flux of photons needed to generate electron holes continuously. An optics module needs to be developed in order to minimize the power required to operate the device and to efficiently relay the light to where it is needed (the photocatalyst) and shield the light from areas where it can potentially cause damage.

4) *Integrated design of all components*

The work discussed in this thesis encompasses goals (1) and (4). Experiments with our design have shown that (a) we can produce a constant flux of O_2 from the photocatalyst over time thus allowing steady-state operation and (b) blood can be fully oxygenated in real time, although only at slow flow rates at present.

1.2 Organization

The thesis will be organized as follows:

Chapter 2 provides relevant background in order to understand how blood oxygenation occurs in vivo and how photocatalysts are employed to produce oxygen, as it relates to the design goals of the microfluidic device for artificial respiration.

Chapter 3 discusses the fabrication of the thin film photocatalyst and its characterization. The goal is to develop a deposition protocol to produce a highly active film.

Chapter 4 proposes a design for a device that incorporates a highly active thin film photocatalyst into a microfluidic chip, details its fabrication procedure and validates device function.

Chapter 5 presents a brief summary of the thesis, discusses ongoing work that is being done on the project, and provides recommendations for future research.

(This page intentionally left blank)

Chapter 2

Background

The microfluidic device for artificial respiration is the result of a complex integration of technologies from various fields. For the proper design of a microfluidic device, the requisite knowledge of biology, biochemistry, materials science, and micro- and nano-fabrication are necessary. For this project, in particular, a brief review of respiration, photocatalysis, and microfluidics is relevant.

2.1 Respiration

Respiration can be divided into two phases: internal and external. Internal, or cellular respiration, is the set of metabolic reactions that takes place in the cells once it has acquired dissolved oxygen gas to convert carbohydrates into biochemical energy. The mechanisms of cellular respiration are well known and are not studied in this work. External, or pulmonary, respiration is of interest at present because most patients of lung disease suffer when pulmonary respiration is affected. The following is a brief, yet critical, overview of the fundamentals of respiration as it pertains to the issues addressed by the device for artificial respiration.

2.1.1 Pulmonary respiration

The function of the lungs is to facilitate gas exchange with the environment—oxygen to venous blood and carbon dioxide out of the body. Although the lungs have other functions (metabolizing compounds and filtering unwanted materials from blood circulation, for example), the main purpose of the organ is to get oxygen to the blood

where it can be taken to the tissues of the body for cellular respiration and release the byproduct, carbon dioxide.

The exchange of oxygen and carbon dioxide relies on a pressure differential and simple gas diffusion through thin membranes. When one inspires, the volume of the thoracic cavity increases because of the displacement of the diaphragm and the rising of the ribs. The pressure in the lung's internal cavity decreases, inducing a rush of air into the airways. The average person breathes in about 4 liters of air into her lungs per minute and the heart pumps approximately 5 liters of blood per minute through the pulmonary cavity.[8] The large volume of fluid, both air and blood, must efficiently undergo an exchange of gases in a short period of time. The unique structure of the lung allows for efficient and rapid oxygen and carbon dioxide exchange.

According to Fick's law of diffusion, the flux of gas transport through a tissue is proportional to surface area and inversely proportional to the thickness of the membranes. The membranes constituting the blood-gas barrier in lungs are very thin (dimensions as small as 0.3 μm in certain areas) and the barrier has a total surface area between 50 and 100 square meters.[9] The average lung, however, only has about 10% solid tissue. Three-hundred million tiny air sacs, called *alveoli*, are responsible for the prodigious surface area and the total volume of the alveoli amounts to 4 liters.[8,9] To provide some perspective, a sphere of the same volume would have a surface area of only 1/100th of a square meter. The alveoli are surrounded by webs of tiny capillaries measuring 5-10 μm in diameter. Since erythrocytes are 6-8 μm in diameter, they enter the capillaries in single file, allowing for a direct path for oxygen diffusion to the cells. Refer to Figure 2.1, an electron micrograph showing a pulmonary capillary (C) that resides in the thin blood-gas barrier. The arrow indicates the diffusion path from the alveoli (the white void) to the erythrocyte (EC), or red blood cell.

As is evident from the micrograph, the membrane through which oxygen must diffuse can be as thin as a 0.3 μm. The diffusion coefficient, D, of a molecule is proportional to

the gas solubility, *Sol*, and inversely proportion to the square of the molecular weight, *MW*:

$$D \propto \frac{Sol}{\sqrt{MW}}$$

The time required for diffusion scales with the square of the membrane thickness, *L*, and the inverse of the diffusion constant:

$$t \sim \frac{L^2}{D}$$

Abnormalities common to lung disease often result in the mucosal thickening of the blood-gas barrier, essentially increasing the value of *L*, thus impeding the diffusion of gases across it. As mentioned previously, chronic sufferers of lung disease often have infections that thicken the layer of viscous fluid in their lungs, making it very difficult for them to breathe.
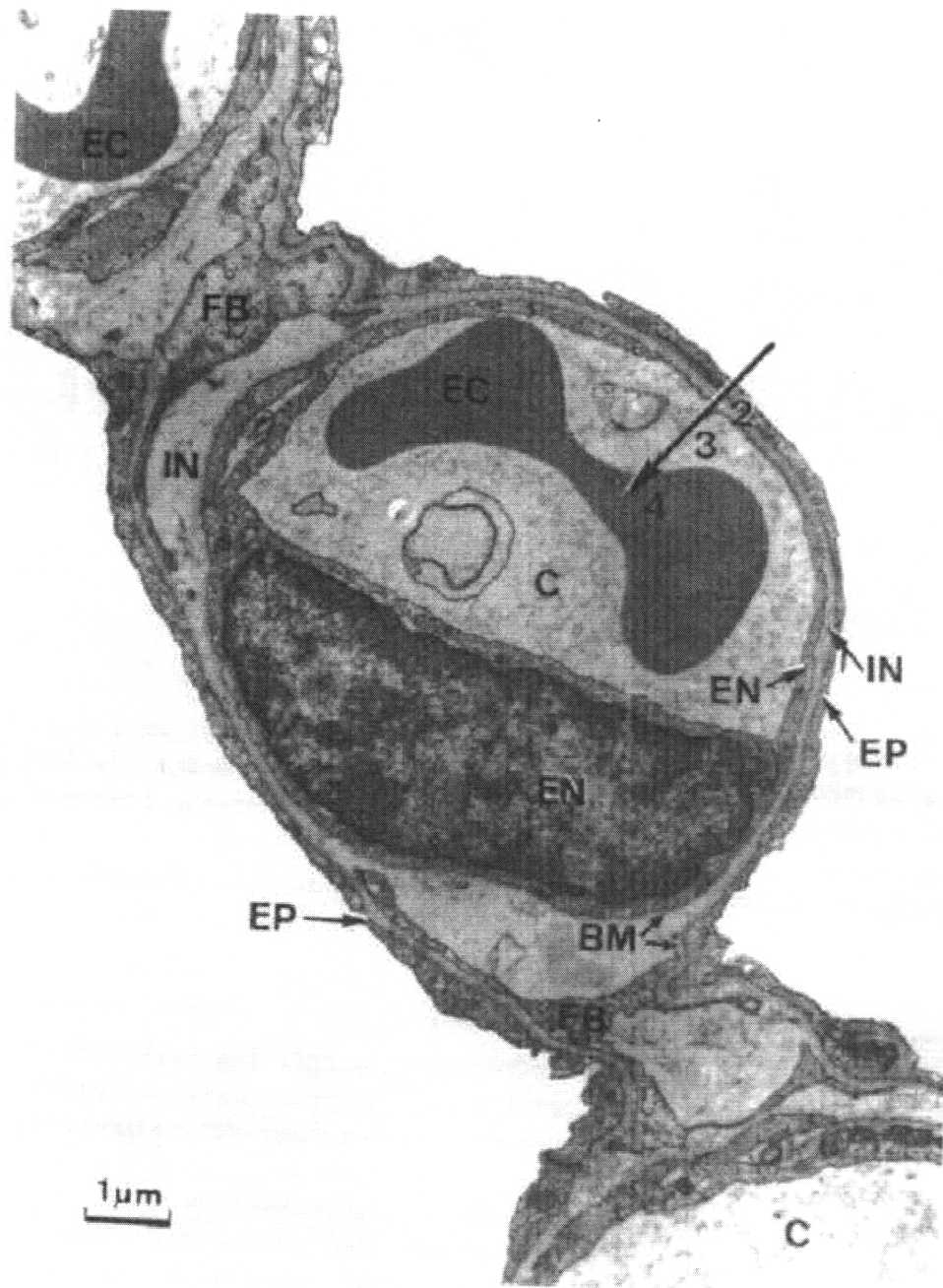
Figure 2.1: Electron micrograph showing a pulmonary capillary in the alveolar wall. [Reproduced from West, 2000]

2.1.2   Blood oxygenation

The structure and function of hemoglobin and myoglobin have been investigated thoroughly by biochemists over the last five decades. They were the first proteins whose three-dimensional structures were determined[10,11] and, as a result, the reversible binding of a protein to ligand is now very well understood. Hemoglobin is a protein residing in red blood cells containing four identical subunits that contains an iron-porphyrin heme group and functions in the transport of oxygen. Myoglobin, although structurally similar to a single subunit of hemoglobin, is the oxygen-storing protein in muscles.

Oxygen has a low solubility in aqueous solutions and cannot be carried to the tissues of the body in sufficient amounts simply by dissolution in blood serum. The solubility of oxygen in blood is only 0.0031 mL O_2/100 mL blood/mm Hg. Small organisms have found it possible to rely solely on the diffusion of oxygen through membranes, but that alone cannot sustain larger multicellular organisms as diffusion is ineffective over distances greater than a few millimeters. Birds and mammals employ hemoglobin by exploiting the strong tendency of oxygen to bind to certain transition metals, like iron and copper.[12] The protein prosthetic group, heme, consists of an organic ring, protoporphyrin, that has a single iron atom in the ferrous state (Fe^{2+}) at its center. Fe^{2+} is capable of binding oxygen reversibly and more than 90% of the oxygen in blood serum is that which is bound to the hemoglobin.

The figure below shows the sigmoidal oxygen affinity curve for hemoglobin. The hemoglobin in blood must bind oxygen efficiently in the lungs, while releasing the oxygen (have decreased affinity for binding) in the tissues of the body. Allosteric proteins, such as hemoglobin, are capable of having variable affinities to ligands because the binding of a ligand to one site causes conformational changes that affect binding to another site. In the case of hemoglobin, there are four binding sites for O_2 and, as more oxygen molecules bind to it, the protein transitions from a low-affinity state to a high-affinity. Therefore, as oxygen binds to hemoglobin in the lungs where the partial pressure, pO_2, is about 13.3 kPa, its affinity increases and more oxygen binds. Conversely, as the erythrocytes move to the tissues where pO_2 is approximately 4 kPa,

oxygen releases itself from hemoglobin and the binding affinity decreases.[12] Figure 2.2 also shows that approximately 10% of the oxygen concentration in blood is dissolved in the plasma, while the other 90% is combined with hemoglobin.
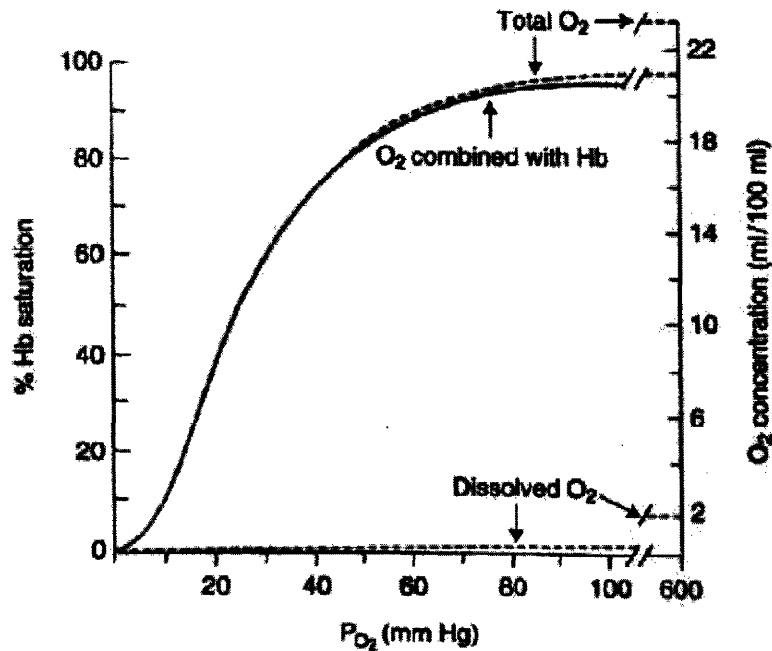
Figure 2.2: O_2 dissociation curve. The solid line is for pH = 7.4, pCO_2 = 40mm Hg, and temperature = 37°C. The dotted line is the oxygen concentration in 100 mL blood. [Reproduced from West, 2000]

Normal erythrocytes (red blood cells) are small biconcave disks (about 6 to 9 μm in diameter) that are vestigial cells, unable to reproduce and survive for more than 120 days.[10] Their sole function is to carry hemoglobin. In arterial blood, hemoglobin is 96% saturated with oxygen and venous blood is about 64% saturated. Therefore, about every 100 mL of blood flowing from the lungs, throughout the body, and then back again releases about 6.5 mL O_2 in the process.[9] This serves as a benchmark for our photocatalyst design as one of the ultimate goals of the microfluidic device for artificial

respiration is to achieve enough oxygen yield from the photocatalytic reaction to sustain cellular respiration in the body.

2.2 Photocatalysis

The breakthrough work of Fujishima and Honda in 1972,[13] in which they achieved ultraviolet light-induced water cleavage with the use of titanium dioxide (TiO_2) in an electrochemical cell, has drawn considerable attention in recent years to the "acceleration of a photoreaction by the presence of a catalyst"[14] or photocatalysis. The possibility of solar energy conversion by semiconductors or sensitizers is of increasing interest because of the current effort to create renewable energy sources to replace the use of fossil fuels. Exhaustion of natural energy sources and environmental pollution has almost necessitated these technological efforts. The amount of solar light impinging on the earth's surface is more than 10^{24} J/year, 10^4 times that of the world's energy consumption.[15,16] Consequently, harnessing solar energy in sustainable and environmentally-friendly processes has become one major effort to decrease the global dependence on fossil fuels.

The need for efficient production of fuels from inexpensive materials and with minimum waste generation has been the motivator for many research projects in energy. An example of simple, and highly desirable, reactions is the oxidation reaction of water into H_2 and O_2 and the reduction of CO_2 into methanol driven by light. The effect of light in these cases is to create electron-hole pairs in catalysts that, like the charge separation in a battery, provide the driving energy for reactions to take place. The analogous model often used for these energy conversion systems is biological photosynthesis.

During the process of photosynthesis, plants and certain species of bacteria capture energy from sunlight and produce useable fuels that help them grow. In this process, CO_2 is reduced to sugar and carbohydrates in a rather complex set of reactions: pigments absorb energy from sunlight, that energy oxidizes water to produce oxygen, and the electrons from the oxidation reaction contribute to the formation of carbohydrates. The

fundamental aspect of the energy conversion process is the removal and then separation of the electrons from their source, H_2O. The separation of charges is accomplished by the presence of very thin lipid membranes in the organelles of plant cells through a series of intermediate redox reactions involving proteins with metal complexes. Photocatalysis essentially replicates this first phase of the photochemical solar energy conversion of photosynthesis – light induced water splitting and charge separation – without carrying out the dark reactions that produce carbohydrates from CO_2. Photosynthesis is the most efficient and successful solar conversion system available, and thus serves as an ideal model for photocatalysis.

2.2.1   Semiconductor photocatalysis

Photocatalysts are used to induce redox reactions because solar energy alone cannot excite electrons of simple molecules to higher energy states. Semiconductors are uniquely positioned to be used as photocatalysts because of their electronic structure. By definition, semiconductors are materials with an electrical conductivity between that of conductors and insulators. Upon illumination of these materials with light having energy greater than the bandgap energy, E_{bg}, electrons from the valence band elevate to higher energy levels leaving behind electron vacancies or "holes". Energy or current is carried by electrons and holes, and the rate at which they move can be precisely tuned by processes like doping, in which impurities are intentionally added to the bulk material to change its electronic structure. The photoexcitation of semiconductors is an effective means of initiating important and normally energetically unfavorable redox reactions.

The overall photocatalysis reaction in a semiconductor is as follows:

$$A + D \xrightarrow{\quad semiconductor + light \geq E_{bg} \quad} A^- + D^+$$
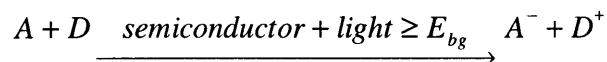
where A is an electron acceptor and D is an electron donor.[14,16] Upon excitation of light with energy greater than E_{bg}, electron-hole pairs can be generated. Either spontaneously

or under the action of an electric field, the electrons and holes generated move in opposite directions, either further into the bulk or to the surface of the photocatalyst, where an electron acceptor can be reduced (refer to Figure 2.3, reaction (c)) and where a donor can be oxidized (Figure 2.3, reaction (d)). Otherwise, recombination of the electron-hole pairs can occur within the bulk, losing the opportunity for their use in any redox reactions. This is of significance because the recombination of electron-holes is a severe limitation in photocatalysis.
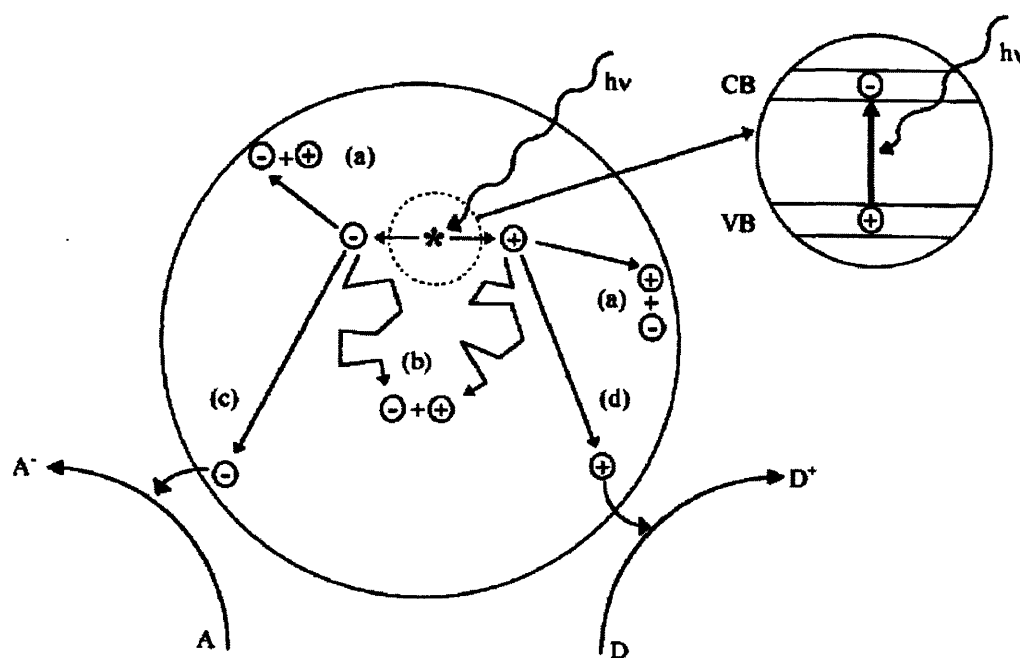
Figure 2.3: Illustration of the major processes occurring on a semiconductor particle following electronic excitation. Electron-hole recombination can occur at the surface (reaction (a)) or in the bulk (reaction (b)) of the semiconductor. At the surface of the particle, photogenerated electrons can reduce an electron acceptor A (reaction (c)) and photogenerated holes can oxidize an electron holes can oxidize an electron donor D (reaction (d)). [Reproduced from Mills and Le Hunte, 1997]

2.2.2   Electron-hole recombination

It is often a challenge to predict the yield of the photocatalytic redox reactions. That is, it is difficult to determine the lifetime of the oxidized and reduced species that form after a semiconductor photocatalyst has been activated by light. Energy absorbed by the material results in the formation of electron-hole pairs but, if the pairs do not migrate far or recombine (reactions (a) and (b) in Figure 2.3) before reaching the surface of the semiconductor, the energy is simply released as heat. Unlike the formation of the electron-hole pairs, it is not easy to predict the recombination rate directly. Photocatalytic semiconductors have generally been found to have low quantum efficiency because the recombination of electron-holes shortly after they are generated predominates the photocatalytic activity.[17] An ordinary semiconductor redox reaction has the efficiency of about 30%, meaning that 70% of the electron-hole pairs that are generated recombine before any reaction takes place.[16] Thus, for the design and proper function of a semiconductor photocatalyst, recombination cannot be ignored.

Research in the field of semiconductor photocatalysis has focused on designing materials with high activity. It is well known that photocatalytic activity depends on the surface area and particle size of semiconductor powders, the material's crystal structure,[14] and adjustment of their bulk properties.[18] The reason these properties have a significant effect on photocatalytic activity is because they each serve to segregate electrons and holes and/or reduce the probability of recombination. As the particle size decreases, the photocatalytic activity of a semiconductor increases due to the increase in surface area to bulk volume ratio. Consequently, redox reactions are induced readily because the diffusion distance (and thus, probability of recombination) for photogenerated electron-hole pairs is minimized. For this reason, photocatalysts are often employed in powder form or, in some instances, as thin films with high surface roughness. As for crystal structure, it has been shown that high crystallinity has the effect of increasing photocatalytic activity in metal oxide semiconductors.[17,19,20] Many studies have shown that annealing improves the crystallinity of photocatalysts and reduces crystal defects—

assumed sites of electron-hole pair recombination.[14.16] The importance of crystal structure will be elaborated upon in a later chapter.

Recently, doping of photocatalytic semiconductors, like TiO_2, has been attempted to manipulate bandgaps such that the materials are highly reactive under visible light.[18,21] Although materials with changed bulk properties suffer from thermal instability and a possible increase of electron-hole recombination centers, it has also been shown that the photocatalytic activity of TiO_2 is remarkably enhanced with the addition of small amounts of noble metals.[18] This is explained by the quick segregation of the electrons and holes, as the electrons are transferred to the metal particles. In the case of photo-induced splitting of water using platinum-loaded TiO_2, for example, the holes are free to oxidize water and the electrons on the Pt participate in H_2 evolution. Recombination, in such a case, is minimized. Figure 2.4 illustrates the decomposition of acetic acid using Pt-loaded TiO_2 particles illuminated by UV light.
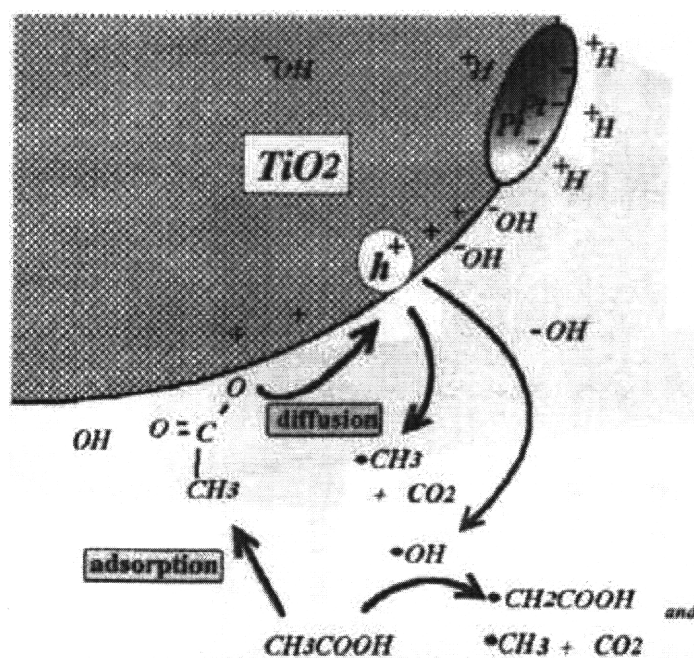
Figure 2.4: Schematic illustration of decomposition of acetic acid. [Reproduced from Kaneko and Okura, 2002]

The principle behind metal loading as a means of reducing the probability of electron-hole recombination can be extended to photoelectrochemical cells. In such cells, instead of adding metal particles to the bulk semiconductor directly, the photocatalyst is connected via an external circuit to a metal electrode (usually made of platinum) through which electrons can be conducted. As presented in the following section, this system can be highly efficient in photocatalytic activity, with quantum yield reaching nearly 100% for some single-crystal semiconductor cells.[16]

2.2.3   Photoelectrochemical cells

The possibility of solar photocatalysis was first demonstrated in the late 1960s by Honda and Fujishima when an n-type TiO$_2$ semiconductor connected to a platinum counterelectrode was exposed to UV light (refer to Figure 2.5).[6] When irradiated with light, current flowed from the platinum electrode to TiO$_2$ through an external circuit. It was shown that oxygen evolution occurred at the TiO$_2$ electrode and hydrogen gas formed on the Pt electrode as per the following water-splitting reactions:

Excitation of TiO$_2$ by light:

$$TiO_2 + 2h\nu \rightarrow 2e^- + 2h^+ \qquad \text{(Eq. 2.1)}$$

At the TiO$_2$ surface:

$$H_2O + 2h^+ \rightarrow \frac{1}{2}O_2 + 2H^+ \qquad \text{(Eq. 2.2)}$$
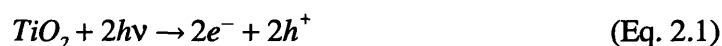
At the counter electrode:

$$2H^+ + 2e^- \rightarrow H_2 \qquad \text{(Eq. 2.3)}$$

The overall reaction is:

$$H_2O + 2h\nu \rightarrow \frac{1}{2}O_2 + H_2 \qquad \text{(Eq. 2.4)}$$

In this preliminary photoelectrochemical cell, no external voltage was applied. When the semiconductor electrode is in contact with an electrolyte, as it is in Figure 2.5, charge

equilibrium takes place at the interface.[16] A charge layer within the region close to the semiconductor bends the electronic energy bands and creates a local electric field, driving photogenerated holes toward the surface of the semiconductor and electrons into the bulk material. In solution, the redox reactions occur readily on the surfaces of the electrodes because the action of the electric field efficiently drives electrons and holes in opposite directions.[22]
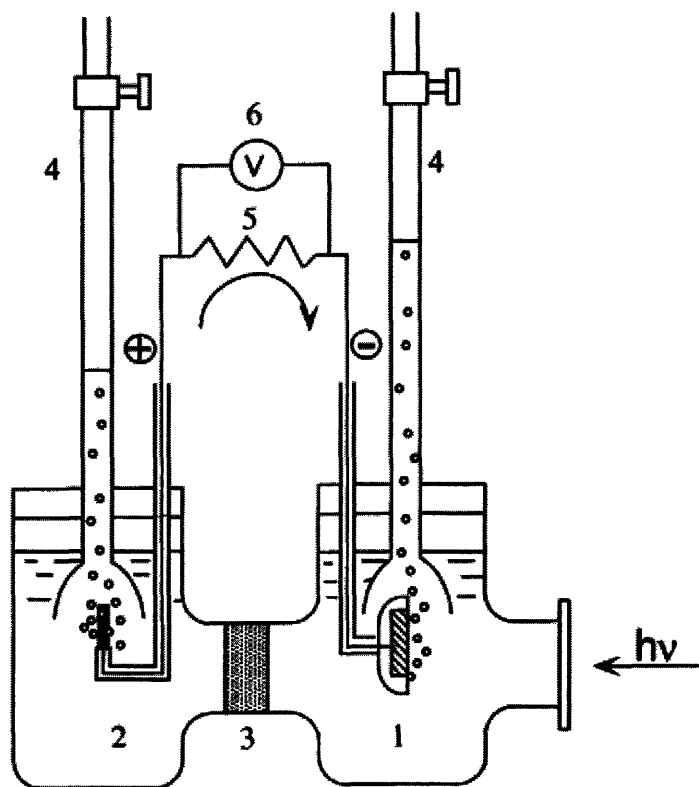
Figure 2.5: Electrochemical cell employing TiO_2 as a photoanode. (1) n-type TiO_2 semiconductor; (2) platinum counter electrode; (3) ionically conducting separator; (4) gas buret; (5) load resistance; (6) voltmeter. [Reproduced from Fujishima, 2000]

The presence of a counter electrode and electrolyte solution are essential for high yield of electron-hole pairs. As in the case of metal-loaded semiconductors, where small amounts of Pt, for example, are added to the bulk material, the counterelectrode serves as the site

for hydrogen evolution. The electrochemical cell used by Fujishima and Honda is a set-up that motivates the design of the photocatalytic cell for artificial respiration.

2.3 Microfluidics

Microfluidics is the manipulation of fluids in micrometer-sized channels, of volumes from 10^{-9} to 10^{-18} liters. The development of so-called labs-on-chips and micro total-analysis systems (μTAS) has aided in the investigation of biological and chemical synthesis and analysis. The field of microfluidics has a wide range of applications, even those extending to optics and information technology. The scales on which these devices are designed lend themselves well to the fabrication techniques of semiconductor and integrated circuit technologies. Additionally, chips can be designed and fabricated rapidly, they are inexpensive and small, and they consume low volumes of samples and reagents. Therefore, microfluidics presents itself novel means of analysis and synthesis on the micro-scale.

The behavior of fluids on this scale can differ significantly from the behavior of "macrofluidics" because factors such as surface tension, energy dissipation, fluidic resistance and electrochemical interactions dictate phenomenon at the micro level. Microfluidics often studies these factors and how they can be exploited experimentally. In microfluidic devices, like the one that is discussed in this thesis, two things hold true: (i) the dimensionless Reynolds number is low and aqueous flow is laminar, not turbulent and (ii) diffusion plays an important role in mass flow because the feature dimensions are small.

In the case of the development of a device for artificial respiration, microfluidics plays an important role. To begin with, the oxygen being produced by the photocatalytic semiconductor is essentially a flux of dissolved gas that comes only from the lower plane of the channel. In order for the oxygen to bind to the red blood cells that are flowing above the photocatalyst, it must diffuse through the height of the channel faster than it is

being advected by the flow. As mentioned earlier, that criterion is fulfilled if the Péclet number is low. Second, the channels that will be molded into the polymers of the ultimate microfluidic device design will have dimensions, geometry and branching similar to that of capillaries. Standard soft lithography techniques will make this a feasible endeavor.

(This page intentionally left blank)

Chapter 3

Film Fabrication and Characterization

Since the 1960s, titanium dioxide has been the focus of research on photocatalysis and there have been many investigations into its various applications. TiO_2 has been found to be non-toxic and mechanically stable, can be fabricated at low-cost, and has a bandgap of approximately 3 eV, ideal for excitation by light in the ultraviolet range. Titanium dioxide employed in aqueous form, in powders and as coatings on surfaces have great oxidative power. So far, the most active application of photocatalysis has been the photodegradation of organic compounds. TiO_2 has been used as a coating for self-cleaning and anti-microbial surfaces in office buildings and hospitals, and in water, air and wastewater treatment systems.[23] Two years ago, an Italian company incorporated TiO_2 into cement to create smog-eating building materials for industrial and urban settings.[24] Titanium dioxide has also been used in anti-fogging coatings because of its superhydrophilicity when activated by UV light[25] and has been employed as a means of killing malignant cancer cells.[26] The application of most interest to this project is the use of the metal oxide semiconductor in solar cells for oxygen and hydrogen production by water splitting.

All of the uses of titanium dioxide in photocatalytic cell applications rely on its high activity once irradiated by UV light. It has been reported that amorphous TiO_2 has negligible activity indicating that crystallinity improves production of electron-holes and impedes recombination. Titanium dioxide exists in three crystal phases: rutile, anatase and brookite. Rutile is the most thermodynamically stable, and anatase exhibits the most photocatalytic activity, while brookite is the rarest and most inactive. Anatase and rutile both have titanium cations coordinated to six oxygen anions in an octahedron, but the

packing of the octahedra differ in the two crystals.[27] The surface areas of anatase crystals tend to be greater than those of rutile as a result, and anatase films are slightly less dense.

The criteria for the titanium dioxide films that are to be employed in the microfluidic device for artificial respiration are as follows:

(1) *High crystallinity*: The concern is not so much the size of the grains, but the percent content of anatase versus other crystal phases. The presence of rutile will decrease the activity of the overall film. Therefore, our goal is to develop a deposition protocol to produce pure anatase thin films.

(2) *Smooth films*: High surface roughness or high porosity, although favorable for the photocatalyzed splitting of water, is undesirable in biomedical applications because of the possibility of cell adhesion and proliferation within the semiconductor. Bio-fouling decreases the affective surface area of the photocatalyst and therefore ought to be minimized.

The overarching goal of the artificial respiration project is to supply oxygen to the blood stream in a closed system. In order produce enough oxygen to saturate red blood cell hemoglobin as it is in normal pulmonary function, the chief aim is to maximize the photocatalyst efficiency of oxygen formation. In the present chapter, the optimization and characterization of titanium dioxide thin films fabricated using two different methods – the sol-gel method and reactive sputtering – have been explored.

3.1 Sol-gel

The sol-gel method is a wet-chemistry technique used primarily for the fabrication of metal oxides. The term refers to the first stage transformation of the "sol" or liquid-like material to a more solid-like "gel". The process involves the following steps: (1) formation of a sol containing an organometallic precursor, usually a metal alkoxide, in solution with alcohol and/or water; (2) aging and deposition of the sol on a substrate; (3) evaporation of the solvents, gel formation, and film solidification; and (4) heat treatment

for the pyrolysis of residual organics, and densification and crystallization of the film.[28] The result is a thin film of metal oxide covalently bonded to the substrate. The reaction is as follows:

$$Ti(OR)_4 + (2+x)\,H_2O \rightarrow TiO_2\,x\,H_2O\left(oxide\ nanoparticle\ attached\ to\ substrate\right) + 4ROH$$

(Eq. 3.1)
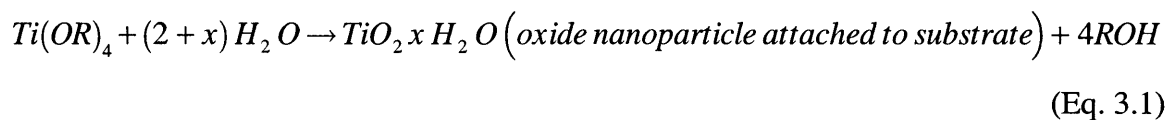
The benefits to using the sol-gel method to deposit titanium dioxide films are that it is cost effective, involves simple process chemistry and equipment, and preparation conditions are tunable. Sol-gel has been used often in applications requiring coatings on large surfaces as a result.

3.1.1   Experiments

The sol was prepared using titanium (IV) isopropoxide (TIP) (Aldrich, 99.999%) metal precursor, acetylacetone (AcA) (Sigma-Aldrich, 99%), anhydrous isopropanol (IPA) (Sigma-Aldrich 99.5%) and de-ionized (DI) water. AcA served as a catalyst[29], while the IPA and DI water was used to dissolve the metal precursor and affect the viscosity of the sol. Anhydrous IPA was used so as to be able to precisely control the molar ratio of water in solution. Measured quantities of each were added in the order indicated while the solution was mixed (with a magnetic mixer) on a balance. It was carried out in room temperature and in a nitrogen-infused glove box to minimize contaminants in the solution. The sol was stored in sealed vials in a dry, ventilated area overnight (up to 12 hours) before being spun on thoroughly cleaned three-inch silicon wafer substrates at 1000 rpm. The cleaning protocol entailed a piranha clean to remove oxide formation on the single crystal silicon, and rinse with methanol and isopropanol to increase hydrophilicity. The films were dried in ambient air for one hour before annealing in a 450°C furnace for two hours. It was determined that the annealing time was sufficient to dehydrate the gel and initiate crystallization.

To develop the appropriate process protocol, the molar ratios of the chemicals were varied accordingly and tested: for every 1 part of TIP, acetylacetone was varied from 1 to 3 parts, isopropanol was added in 1, 5, 9, 10, 12, or 14 parts, and the DI water was added in 1 part. Below is the list of samples produced with their TIP: AcA: IPA: H_2O ratios.

Table 3.1: Sol-gel sample matrix, ratios of TIP: AcA: IPA: H_2O

1:1:3:1	1:1:5:1	1:1:9:1			
1:2:3:1	1:2:5:1	1:2:9:1	1:2:10:1	1:2:12:1	1:2:14:1
1:3:3:1	1:3:5:1	1:3:9:1	1:3:10:1	1:3:12:1	1:3:14:1

After annealing, the crystalline structures of the films were studied by glancing incidence X-ray diffraction (XRD). XRD is a technique used to non-destructively reveal information about the crystallographic structure of a material. The material is bombarded with a parallel, monochromatic X-ray beam and the atoms in the lattice structure scatter the waves in diffraction patterns particular to the type of crystal being analyzed. When thin films are deposited on substrates, it becomes necessary to perform glancing incidence (GI) XRD because the contribution to the diffraction pattern from the substrate overshadows that of the film. GIXRD entails shallow angles of incidence and a longer period of scattered wave detection as the signal detected is small for thin materials.

XRD measurements were carried out using a PANalytical X'Pert PRO Diffractometer with monochromated Cu Kα (λ= 0.1540598) incident radiation. Because glancing incidence XRD was performed, the beam was incident at a shallow angle and the signal was collected from 20° to 60° 2θ. The scan was taken at a rate of 0.0089° (2θ) per second in order to obtain as many data points as possible from the thin film. The various instrument parameters were programmed into the diffractometer using the X'Pert PRO Data Collector software. After each 1 hour 15 minute scan, the Data Collector outputted the diffraction pattern and it was compared to those of known, pure crystalline forms of TiO_2 (anatase, rutile and brookite) found in the XRD database. For all the patterns of the

samples tested, none exhibited any presence of brookite as expected and, therefore, the reference pattern for brookite was not included in the figures following.

3.1.2   Results and discussion

The figures below are diffraction patterns of representative samples with TIP: AcA: IPA: H_2O ratios in Table 3.1. Not all the sol-gel solutions that were mixed successfully yielded films. The samples that contained only one part AcA, ratios 1:1:3:1, 1:1:5:1, and 1:1:9:1, spun onto the Si wafers but after the sintering and annealing step, it was found that adhesion of the resulting film was very poor. The films were peeling off the substrate. A likely cause was that there was insufficient acetylacetone to catalyze the reaction in Eq. 3.1, the alkoxides were not cleaved and, as a result, no covalent bonds formed between the titanium dioxide and Si substrate. The samples with three parts IPA, ratios 1:2:3:1 and 1:3:3:1, were found to be too cracked after the annealing step to be tested with the XRD. It was determined that the cause was the fact that the films were too viscous (this was found to be true while the sol-gel was being spun onto the Si substrates) and the evaporation of solvents during the sintering step caused enough stress in the film to produce cracks. To circumvent this problem, sol-gel solutions with higher IPA content were produced.

Figures 3.1, 3.2 and 3.3 shows the diffraction patterns of the films that were successfully produced using the sol-gel process and exhibited sufficient crystallization. In Figure 3.1, samples with 5 parts IPA, ratios 1:2:5:1 and 1:3:5:1 are compared to the peak locations and relative peak intensities of pure rutile and anatase below the diffraction patterns. For rutile TiO_2, peak locations are at $2\theta = 27.4°, 36.1°, 39.2°, 41.2°, 44.1°, 54.3°$ and $56.6°$ and for anatase, the peak locations are at $2\theta = 25.3°, 36.9°, 37.8°, 38.6°, 48.1°, 53.9°$ and 55.1. As can be seen in the figure, the dominant crystal phase in 1:2:5:1 is rutile while there are only trace amounts of anatase (i.e. only the first, major anatase peak (101) appears in the diffraction pattern). It is also noted that the peaks have relatively low signal intensities indicating that there was not very much crystalline material in the film. Sample 1:3:5:1, on the other hand, exhibits anatase TiO_2 with trace amounts of rutile.

Both diffraction patterns show that there is a significant amount of amorphous TiO_2 in addition to the rutile and anatase crystal phases. This is indicated by the broad peak that occurs near $2\theta = 29°$.
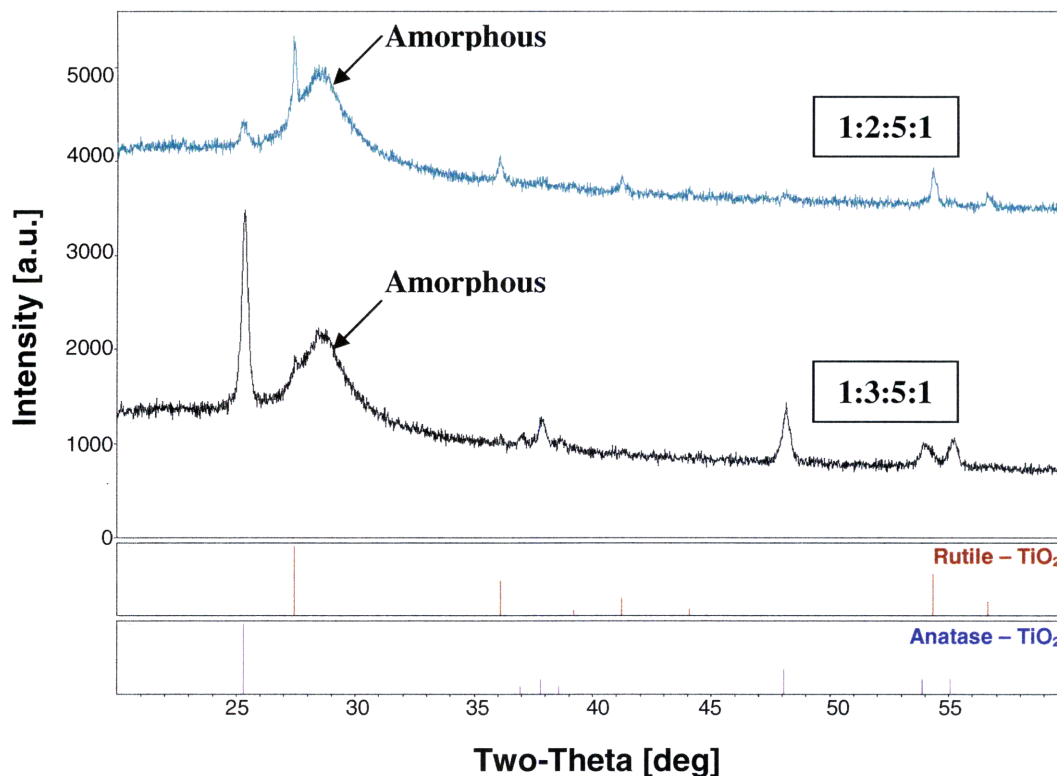
Figure 3.1: XRD patterns of sol-gel samples made in ratios 1:2:5:1 and 1:3:5:1.

The samples 1:2:5:1 and 1:3:5:1 showed promising results, but the presence of amorphous TiO_2 and cracking exhibited by the films was not acceptable for future use in the microfluidic device. The amorphous content can be explained by the fact that the sol-gel solution was viscous and, as a result, too thick for the annealing step to sufficiently crystallize the film. As mentioned earlier, it is necessary that the TiO_2 films be smooth to prevent cell adhesion to the catalyst surface and clotting. Sol-gel mixtures were made

with increased IPA in solution while maintaining the same amount of TIP, AcA and DI
water to see if the dilutions would decrease the viscosity and address the cracking
problem.

In Figure 3.2, the diffraction patterns of samples 1:2:9:1, 1:2:10:1, 1:2:12:1 and 1:2:14:1
were compared to the reference peaks of rutile and anatase TiO_2. Figure 3.3 shows the
patterns of samples 1:3:9:1, 1:3:10:1, 1:3:12:1 and 1:3:14:1. While the samples exhibited
no cracking or peeling and were highly crystalline, all the diffraction patterns show that
there is significant amount of rutile TiO_2 in each sample. Comparatively small traces of
anatase exist, but not enough for the films to have high catalytic activity. The goal is to
produce a film with 100% anatase content. It is possible that because the sol-gel solution
is diluted with large amounts of alcohol, the crystallization process is affected by the
evaporation of these solvents. With the sol-gel process, as it was carried out in these
experiments, the options are between low-crystallinity, cracked anatase TiO_2 and highly-
crystalline, well-formed rutile thin films.
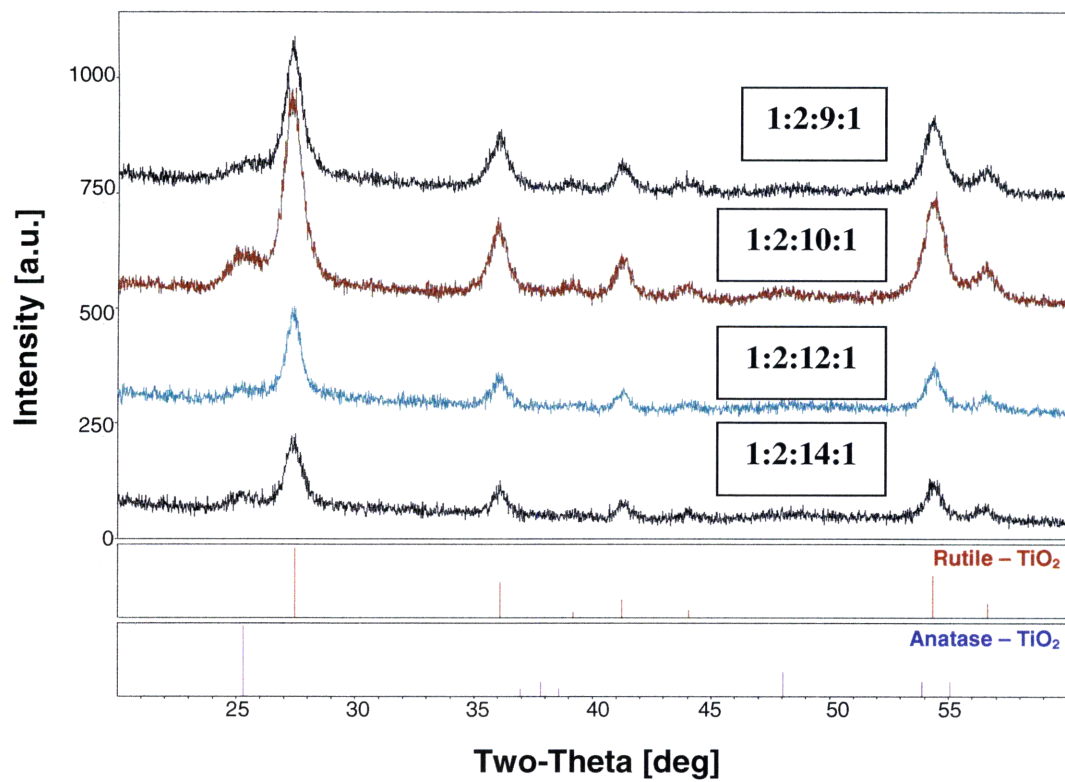
Figure 3.2: XRD patterns of sol-gel samples 1:2:9:1, 1:2:10:1, 1:2:12:1, 1:2:14:1.
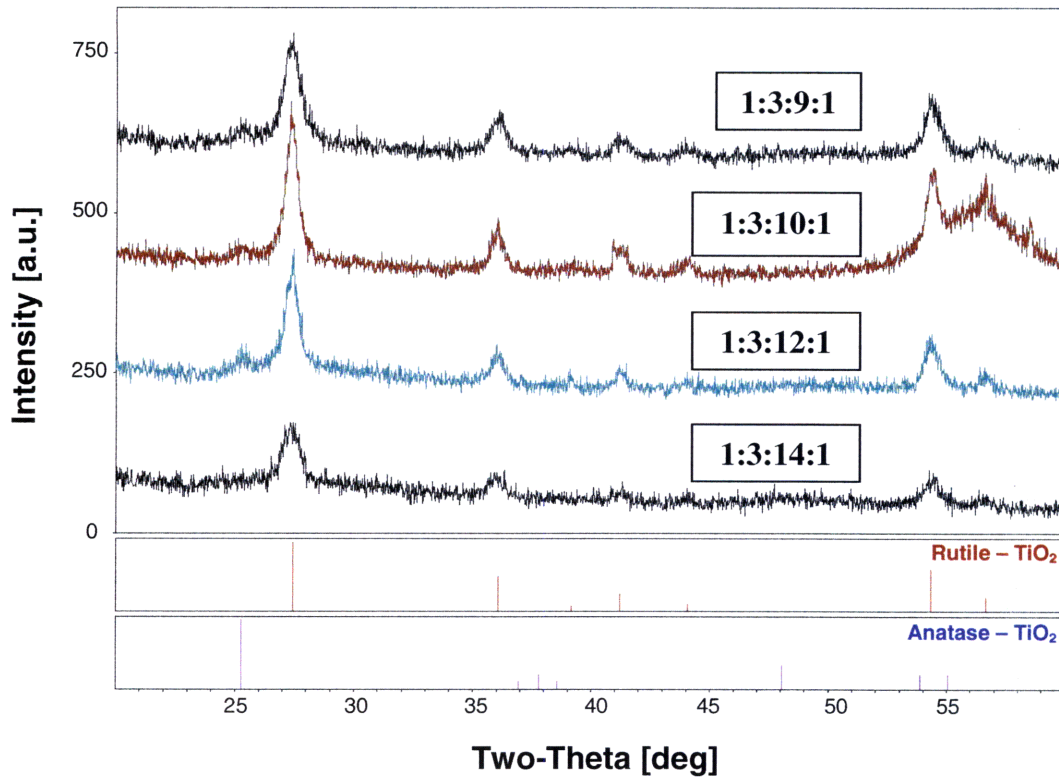
Figure 3.3: XRD patterns of sol-gel samples 1:3:9:1, 1:3:10:1, 1:3:12:1, 1:3:14:1.

3.2 Reactive D.C. magnetron sputtering

Sol-gel has proven to have its limitations in producing the requisite crystalline TiO_2 films. Consequently, reactive D.C. magnetron sputtering was explored as an alternative method. Of the various physical deposition methods that are currently used, among them evaporation, ion beams techniques and chemical vapor deposition (CVD), reactive sputtering holds promise because of the high quality films that can be fabricated. In reactive D.C. magnetron sputtering, a magnetron utilizes an electric field to trap ions close to a metal target, inert gases in the chamber accelerate toward the surface of the target, and it is eroded. The metal particles then interact with the oxygen present in the chamber and the metal oxide molecules are deposited on the substrate. Reactive

sputtering generally forms amorphous films due to the impact of high energy molecules on film growth and the process involves slow deposition rates (on the order of 1 Å/s). However, a post-anneal step crystallizes the titanium dioxide very well and films produced using this method are particularly robust.

3.2.1   Experiments

The titanium dioxide films produced for these experiments were done using an AJA International, Inc. (N. Scituate, MA) Orion 5 high-vacuum sputtering system. The vacuum chamber accommodated three magnetron guns – two RF and one DC – although only the DC gun was used. A substrate holder for substrates of 100mm in diameter was heated to temperatures ranging from room temperature (~25°C) to 100°C. The target was a titanium disk (2 in diameter, purity 99.9%) connected to a mechanism for water-cooling. Two gases—argon and oxygen—flowed through the chamber with the oxygen content ranging from 10% to 20%. The chamber pressure varied between 1.6mTorr and 3.6 mTorr and was controlled by a turbo pump operating at a pumping speed of 1000 Hz and the changing orifice of a throttle valve. The power supplied to the targets remained constant at 250W. The film deposition was always carried out in reactive mode, with oxygen always present in the deposition chamber. In this way, metal oxides of controlled stochiometry can be stably deposited. Table 3.1 below shows the test array for the experiments described.

The films were deposited on 3-inch single crystal silicon wafers and annealed for one hour in a 450°C anneal furnace in order to crystallize the films. The samples were then tested using glancing incidence X-ray diffraction (GIXRD) using the same procedure that was used for testing the sol-gel samples. Included in the table are the deposition rates measured by the quartz crystal monitor (QCM) located in the sputtering unit prior to depositing the films. All films were deposited such that the thickness was maintained at 50 nm. This proved thick enough to obtain a good diffraction pattern, with lots of signal received from the sample, yet was not so thick that long deposition times were required. In the next section, the results of the experiments are discussed and compared.

Table 3.2: Test array for film deposition experiments

Sample	Deposition Pressure [mTorr]	% O_2 in Argon	Temperature [°C]	Deposition Rate [Å/s]
1	1.6	5	RT	2.2
2	1.6	10	RT	2.1
3	1.6	15	RT	1.9
4	1.6	15	50	1.9
5	1.6	15	75	1.9
6	1.6	15	100	1.9
7	1.6	20	RT	1.6
8	2.6	15	RT	1.6
9	3.6	15	RT	1.5
10	3.6	15	50	1.3
11	3.6	15	75	1.4
12	3.6	15	100	1.4

3.2.3   Results and discussion

The figure below shows the diffraction patterns for samples 3, 8 and 9, under varying deposition pressures, 15% O_2 content in the chamber and with room temperature substrates. In literature, it is reported that high vacuum deposition is essential for anatase formation, but the exact deposition pressure recommended varies. Löbl and colleagues suggest a chamber pressure equal or less than 0.7 Pa or 5.25 mTorr.[30] All films under 5.25 mTorr in the experiments that were carried out in Löbl's study crystallized to pure anatase after annealing. Therefore, in these experiments, deposition pressures of 1.6 mTorr, 2.6 mTorr, and 3.6 mTorr were chosen. The measured film deposition rate for pressures below 1.6 mTorr was too low to consider for film fabrication.
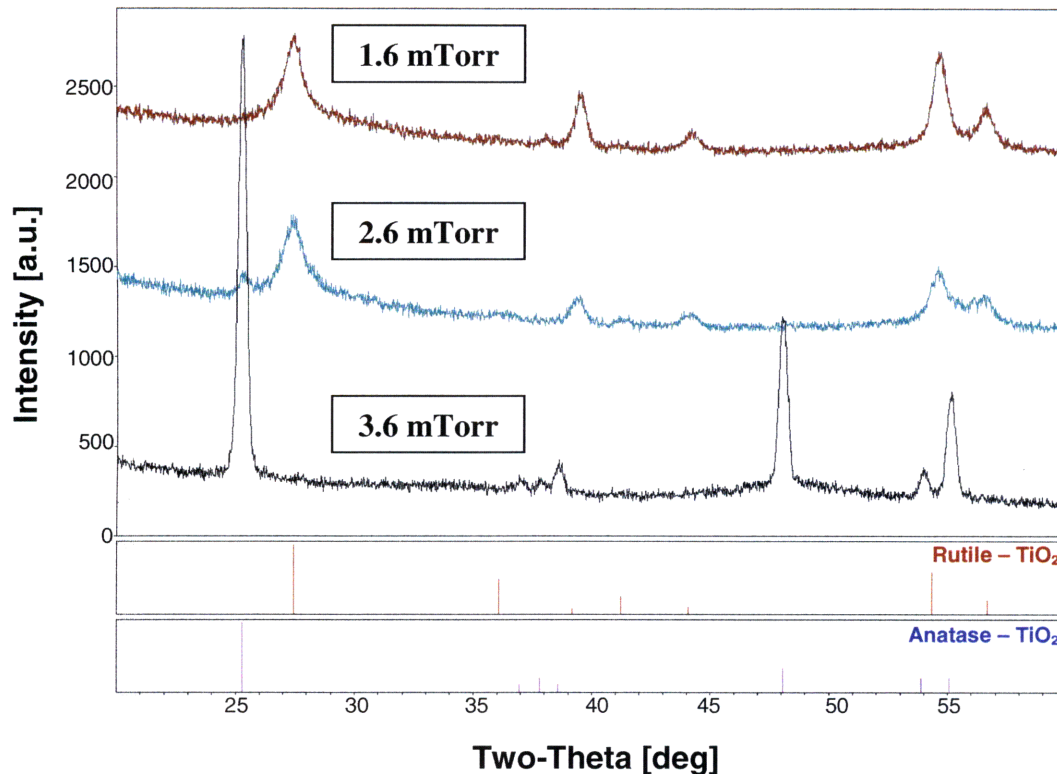
Figure 3.4: XRD patterns of sputtered samples of varying deposition pressure.

Figure 3.4 clearly illustrates that a deposition pressure of 3.6 mTorr yields pure anatase TiO_2. At pressures lower than 3.6 mTorr, the rutile content increases and anatase decreases. The increase in rutile content could possibly be explained by the following reasoning: At very low pressures, the Ti ions interact with the oxygen in the chamber and bombard the substrate with high energy. It is known that the energy of the metal oxide particles being deposited has an effect on how the crystals form in the film. The higher the energy of the particles, the higher the rutile content will be. Another point to note is that, in all the sputtered films, there is no amorphous TiO_2 and almost the whole film is crystallized. This differs from the sol-gel experiments in which there was amorphous content. In fact, the film deposited at 3.6 mTorr exhibits very high crystallinity because the peaks in the diffraction pattern are relatively high and narrow.

The deposition system that was used allowed for sample heating to temperatures up to 800°C. We investigated the effect of sample temperature on the crystallization of the TiO_2 films. Since as-deposited titanium dioxide films are generally amorphous and annealing causes crystallization, it was hypothesized that a heated sample could promote the growth of anatase as deposition occurred and a post-anneal step would not be necessary. After the samples were deposited, our hypothesis proved incorrect; sample heating also resulted in amorphous films as-deposited. We annealed the samples and three diffraction patterns from the resulting films are shown in the following figure.

Figure 3.5 shows the effect of sample temperature on crystallization. As it turns out, the higher the sample temperature, the more rutile TiO_2 forms after annealing. The film sputtered at room temperature showed the best results, with all of the film exhibiting pure anatase crystallization. It seems that the nucleation of rutile TiO_2 is favored when the impinging titanium dioxide particles, formed reactively in the region between the Ti target and sample, have high energies. The formation of rutile is also promoted by the presence of Ti atoms in the vapor phase, which is possible at higher sample temperatures.
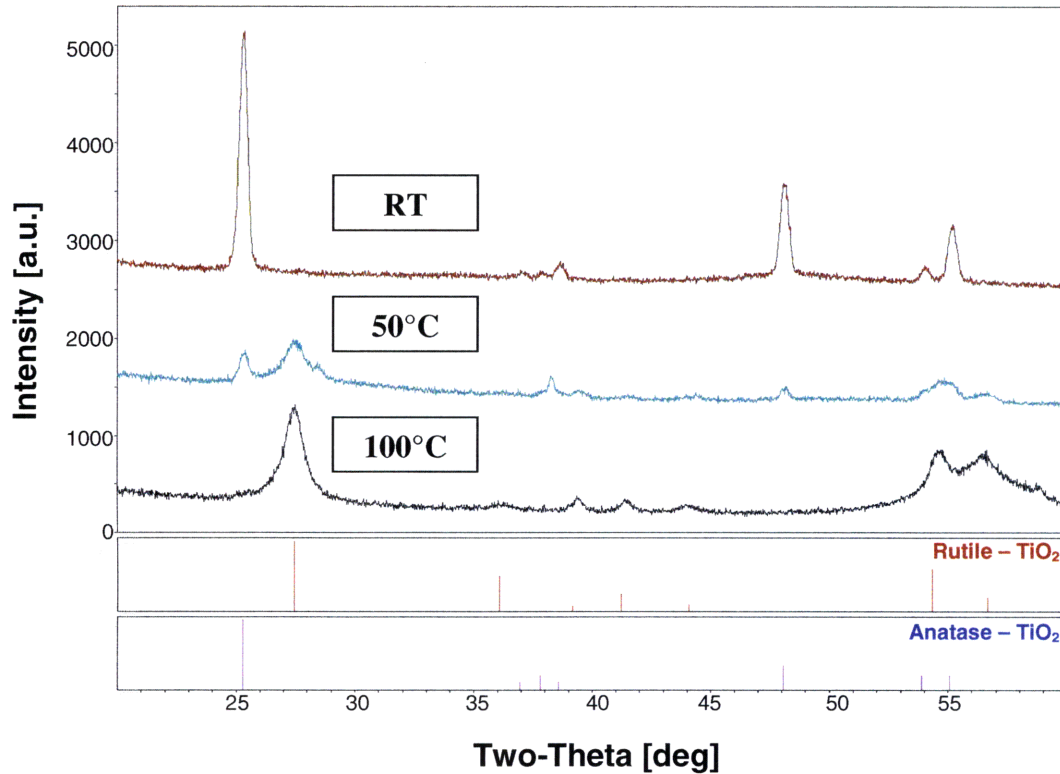
Figure 3.5: XRD patterns of sputtered samples of varying sample temperature.

Figure 3.6 shows the diffraction patterns of films deposited under 10%, 15% and 20% oxygen content, at a deposition pressure of 1.6 mTorr and on samples at room temperature. It has been shown that films sputtered at 1.6 mTorr form rutile when the oxygen content is 10%, but the patterns shown below indicated that increasing the ratio of oxygen to inert gas (Ar in this case) favors the formation of anatase after films are annealed. As mentioned earlier, nucleation of rutile is promoted by the presence of Ti in vapor phase in the vicinity of the substrate onto while the titanium dioxide is being deposited. Increasing the ratio thus favors anatase formation because the Ti vapor is minimized. The results below illustrate, however, that much more oxygen is required to produce pure anatase and to obtain films of high crystallinity.
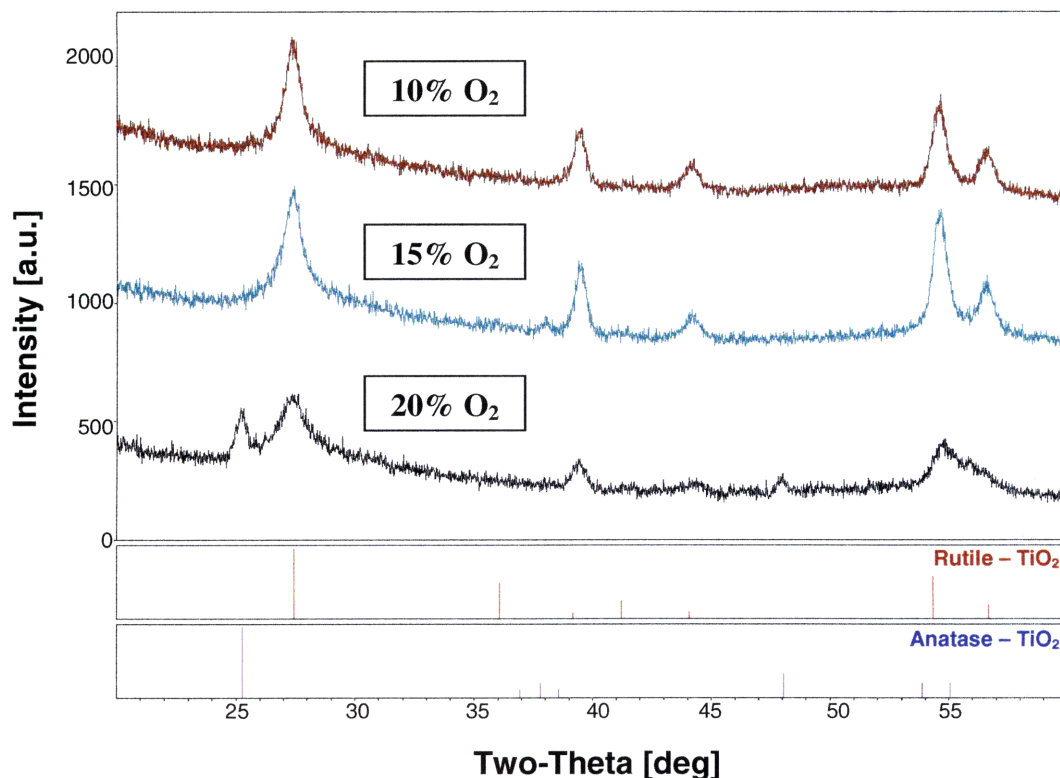
Figure 3.6: XRD pattern of sputtered samples of varying oxygen content.

3.3 Conclusions

The experiments discussed in this chapter compare two different methods of titanium dioxide film deposition. Sol-gel and reactive sputtering, one a wet-chemical technique and the other a physical deposition method, were found to yield very different products. Although sol-gel is an inexpensive and quick means of producing metal oxide films, it was deemed difficult to obtain films that fit both criteria that were outlined in the beginning of the chapter – highly crystalline anatase TiO_2 and smooth films. Although a wet-chemistry protocol is easier to follow, there were several complications encountered because the viscosity of the sol-gel solution, solvent evaporation and crystallization were difficult to control.

The preparation of titanium dioxide thin films using a sol-gel protocol was abandoned for a more expensive and time-consuming process. Sputtering, however, has been found to yield thin films that were mechanically robust and highly crystalline anatase in composition. After performing the experiments, the protocol that was settled on was that which formed the film of sample 9 in Table 3.1. The films were deposited using reactive D.C. magnetron sputtering, at a power of 250W, under a deposition pressure of 3.6 mTorr, in a chamber that contained 15% O_2 and 85% Ar gas and at room temperature. The deposition rate remained roughly at 1.5 Å/s. In Chapter 4, the next steps – where the anatase titanium dioxide thin film developed is incorporated into a microfluidic device for blood oxygenation – are discussed.

Chapter 4

Microfluidic Device Design and Experimentation

In recent years, researchers have been investigating the possibility of using photocatalytic oxygen generation to address deficiencies in pulmonary respiration.[31,32,33,34] In particular, efforts have been made to reproduce a photoelectrochemical cell in a fluidic device for blood oxygenation. In Chapter 2, the mechanism by which oxygen is produced in such a cell, as well as how blood oxygenation occurs *in vivo*, were reviewed. In Chapter 3, the photocatalyst film fabrication was explored. The present chapter describes the design of the novel microfluidic device that is proposed and the experimental work that validates its function.

The novel approach outlined here can be used to oxygenate whole blood and treat patients with chronic and end-stage lung disease in real time. The goal is to create a self-contained, mobile oxygen supply suitable for implantation in patients that will reduce the complications they suffer from current treatments. Specifically, we focused on the development of a highly efficient photocatalytic cell (PC) with the ability to continuously oxygenate venous blood under steady-state conditions.

At the time the work discussed in this thesis was conducted, the only other researchers investigating photocatalytic blood oxygenation were A. Subrahmanyam and his colleagues at the Department of Physics in the Indian Institute of Technology in Chennai, India. Our approach to the artificial respiration differs in several ways from theirs. First, we are the first to integrate the photocatalytic semiconductor thin film into microfluidics. The use of soft polymers, like polydimethylsiloxane (PDMS), in a device is beneficial because of its biocompatibility and ease with which it can be molded into various channel

geometries. Second, the ultimate design of the microfluidic device for artificial respiration will be implanted *in vivo* and blood will be flowing continuously through it by the pumping power supplied by the heart. Therefore, the transport of oxygen to the blood is done in real-time, as it is in normal pulmonary function. The Subrahmanyam design has the blood remaining stationary in a reservoir while photocatalysis takes place.
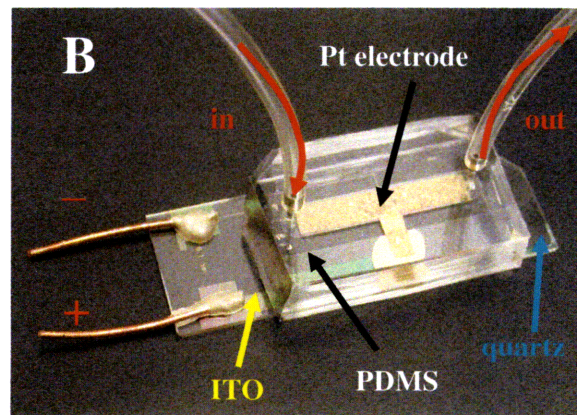
Our device design is outlined as follows.

4.1 Photocatalytic cell (PC) design and fabrication

The photocatalytic cell that was designed is illustrated in Figure 4.1. It is composed of three main components:

(1) a highly crystalline anatase TiO_2 thin film deposited onto a conducting indium tin oxide (ITO) thin film to form a semiconducting junction of TiO_2/ITO,

(2) a platinum (Pt) electrode that is exposed to blood flowing through the channel and by means of which a bias potential can be maintained, and

(3) microfluidic channels molded out of polydimethylsiloxane (PDMS)

The blood flowing in the microfluidic channel is in direct contact with the TiO_2 film, and water in blood plasma (more than 90% of which is water by volume) is oxidized to produce dissolved oxygen gas. During the fabrication process, TiO_2 is sputtered onto a conductive ITO film that has already been deposited on the quartz substrate. Above the fluidic channel is a platinum electrode that is deposited onto PDMS. Between the ITO and Pt electrode, a bias potential is maintained to enhance the migration of electron vacancies, or holes, to the photocatalyst/fluid interface so that oxidation reactions can take place there. The bias also conducts away the electrons generated in the bulk of the photocatalyst when the holes are created. The set-up of the cell in Figure 4.1 is analogous to the photoelectrochemical cell in Figure 2.5 in Chapter 2.

A

bias voltage

channel molded in PDMS

inlet

oulet

Pt electrode film

ITO thin film

quartz wafer

UV

TiO_2 thin film

B

Pt electrode

in

out

−

+

quartz

ITO

PDMS
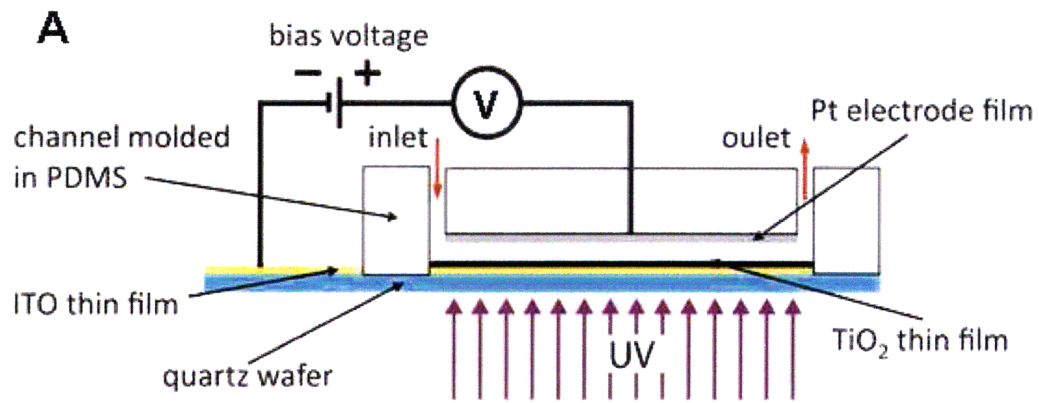
Figure 4.1: A) Schematic and B) photo of assembled device.

4.1.1 ITO/TiO$_2$ thin film deposition

The metal oxide thin films were deposited onto three-inch diameter quartz wafers (Mark Optics Inc., Santa Ana, CA) which served as the substrates for the microfluidic devices. Quartz glass (thickness of 700 μm ± 100 μm) was chosen because it has a transmittance of approximately 96% in the UV range. Indium tin oxide was chosen for the conductive layer because it has a 90% transmittance of UV light and a conductivity of about 10^4 S/cm. The operation of the device relies on the irradiation of the photocatalyst and, as shown in Figure 4.1A, the UV light must pass through the glass and ITO film before it reaches the TiO$_2$ film. Therefore, a high transmittance for both materials is necessary.

As can also be seen from Figure 4.1A, the bias voltage that is applied across the channel relies on closing the circuit between the Pt electrode and the ITO layer. ITO was patterned onto the substrate according the schematic in Figure 4.2. TiO$_2$ was patterned only in the channel region where it is exposed to the blood. The channel for the design of this proof-of-concept microfluidic device is simply rectangular, 4.5 mm in width and 25 mm in length, as the goal was to demonstrate device's capability of blood oxygenation. The minus (-) sign in the figure below indicates that the anode of the electrical circuit is the ITO film underneath the photocatalyst. Once the microfluidic device is assembled, the Pt electrode (which serves as the cathode) will be connected to the U-shaped ITO film that is denoted by the plus (+) sign in the figure below.
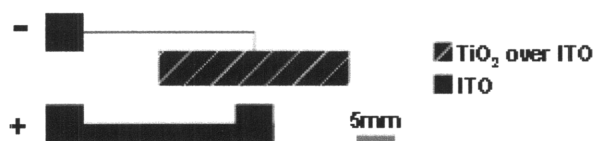
Figure 4.2: Schematic of patterned ITO and TiO$_2$ thin films. The (-) and (+) signs refer to regions where electrical connections were made to close the electrical circuit.

Patterning of the thin films was deemed necessary because, in previous designs, the metal oxides were deposited onto the whole surface of the quartz and bonding was found to be poor between the PDMS and substrate. Patterning has proven to be successful because it allows the polymer to be plasma bonded directly to the glass.

The film deposition protocols of the ITO and TiO_2 are largely covered in Appendix A. To summarize, each quartz wafer was cleaned and a photolithography protocol was carried out to mask with photoresist the area in the negative of what is shown in Figure 4.2. The substrates were then placed in the sputtering unit for metal oxide deposition. The main challenge encountered during fabrication was the drying, cracking and hard-baking of the photoresist due to ion-bombardment and raised temperatures in the sputtering chamber. The substrates underwent two rounds of sputtering amounting to approximately one hour in the chamber. After metal deposition, hard-baked photoresist cannot be removed easily under standard protocol, requiring ultrasonication in a resist remover bath of up to 6 hours or, in some instances, overnight.

Two photoresists were tested to determine what would work best to circumvent this problem. The first, NR7-3000P (Futurrex, Inc., Franklin, NJ), is a negative photoresist chosen because it has a temperature resistance of up to 180°C and can be removed easily with Resist Remover RR4 (Futurrex, Inc.). A test wafer patterned with 3-μm-thick NR7-3000P was sputtered with 200 nm of indium tin oxide and 50 nm of titanium dioxide, at a temperature well below 180°C, and it was discovered that the NR7-3000P was hard-baked. Ultrasonicating the test wafer overnight did not remove the resist. It is presumed that the resist was too thin, and with the deposition of the metal oxide films over the resist, the remover could not lift it off.

The second resist that was tested was AZ-4620 (Shipley, Corp., Somerville, NJ), a positive resist that is used often when an ultra-thick film is required for single-coat processes. This resist was spun onto the test wafer to a thickness of 10 μm and after the photolithography steps, it was kept in a 90°C, humid chamber. The resist thickness, as well as its increased moisture content, yielded a positive result. Following the sputtering

of thin films on the test wafer (200 nm of ITO and 50 nm of TiO_2), the resist was completely removed after five minutes of ultrasonication in an acetone bath. A possible cause is that, during resist development, an undercut formed around the features, and resist remover was able to flow underneath and lift off the resist. As a result of its success, the positive photoresist AZ-4620 was used to mask future quartz substrates for ITO and TiO_2 deposition. The protocol for the lithography steps above are elaborated upon in Appendix A.

4.1.2   Electrode fabrication

To apply the bias voltage across the ITO/TiO_2 junction, a platinum electrode of the same dimensions of the thin metal oxide films (4.5 mm (w) x 25 mm (l)) was deposited onto PDMS above the channel. It is in direct contact with the blood. To fabricate the electrodes, pieces of PDMS (25 mm (w) x 35 mm (l) x 5 mm (h)) were prepared using an elastomer and curing agent (Sylgard 184, Dow Corning) mixed to a ratio of 15:1, respectively, and they were hard-baked overnight at 80°C. Thin masks (~0.5 mm) were made by spinning (475 rpm) PDMS mixed to a elastomer : curing agent ratio of 10:1 onto a clean silicon wafer, baking at 80°C and cutting out the shape of the electrode. The masks were thermally bonded to the hard-baked PDMS for 15 min, again at 80°C. The metal deposition was performed using the same sputtering unit as was used for the ITO and TiO_2 deposition, the AJA International, Inc. (N. Scituate, MA) Orion 5 high-vacuum sputtering system. The details of the metal deposition are included in Appendix A.

Sputtering metals onto PDMS, much less masking of substrates with thin PDMS films, is not standard practice. There were some challenges that were faced to fabricate a thin film electrode on a polymer using a physical deposition process. As mentioned earlier the temperatures of substrates within a sputtering chamber rise, and since PDMS is a polymer the expansion and then shrinkage after metal deposition causes cracking. A cracked electrode decreases the lifetime of the microfluidic device because it shorts the circuit that maintains the bias voltage. The PDMS was hard-baked in order to circumvent this problem, as it made the polymer stiffer. Before deposition of the Pt (of a thickness of 320

nm), a thin 30 nm layer of Ti was deposited to promote the adhesion of the platinum to the PDMS. Both improvements decreased the cracking significantly and produced smooth metal film electrodes. After the metal deposition, the thin PDMS mask was peeled off to reveal the electrode in the "T" shape shown in Figure 4.3(d). The "leg" of the T is the extension that is connected to the ITO film, the cathode of the photocatalytic cell. Figure 4.3(a-d) illustrates the steps of the platinum electrode fabrication.

4.1.3   Channel fabrication

In standard soft lithography, channels are often molded out of bulk PDMS by casting the pre-baked polymer against a mold generating a negative replica. For the purposes of this design, the channels are instead fabricated in the following manner: SU-8 (Microchem, Newton, MA) molds contain the outlines of the channel in positive relief, with the features at 100 µm in height. As mentioned earlier, the channel is simply rectangular in geometry: 4.5 mm (w), 25 mm (l) and 100 µm (0.1 mm) (h). PDMS (Sylgard 184, Dow Corning), mixed in a 10:1 ratio of elastomer to curing agent, was spun onto the molds to a thickness of 100µm. After curing, the solidified PDMS within the channel region was peeled away to create a void through which the fluid flows. When assembling the device, this PDMS "gasket" was sandwiched between the platinum electrode and the glass substrate to form an enclosed channel. Figure 4.3 (e-h) illustrates the major steps of the soft lithography process. Further fabrication details are discussed in Appendix A.

4.1.4   Device assembly

The photocatalytic cell was assembled according to the depiction in Figure 4.3, steps (i) through (k). The electrode deposited on PDMS was aligned onto the channel and plasma bonded, (i); the assembly was baked at 80°C for 5 min and gently peeled off the mold, (j); and the holes to provide inlet and outlet ports to the fluidic device were punched into the PDMS (not shown), the channel assembly was aligned onto the titanium dioxide on the quartz substrate, and the device was plasma bonded. In order to connect the electrode
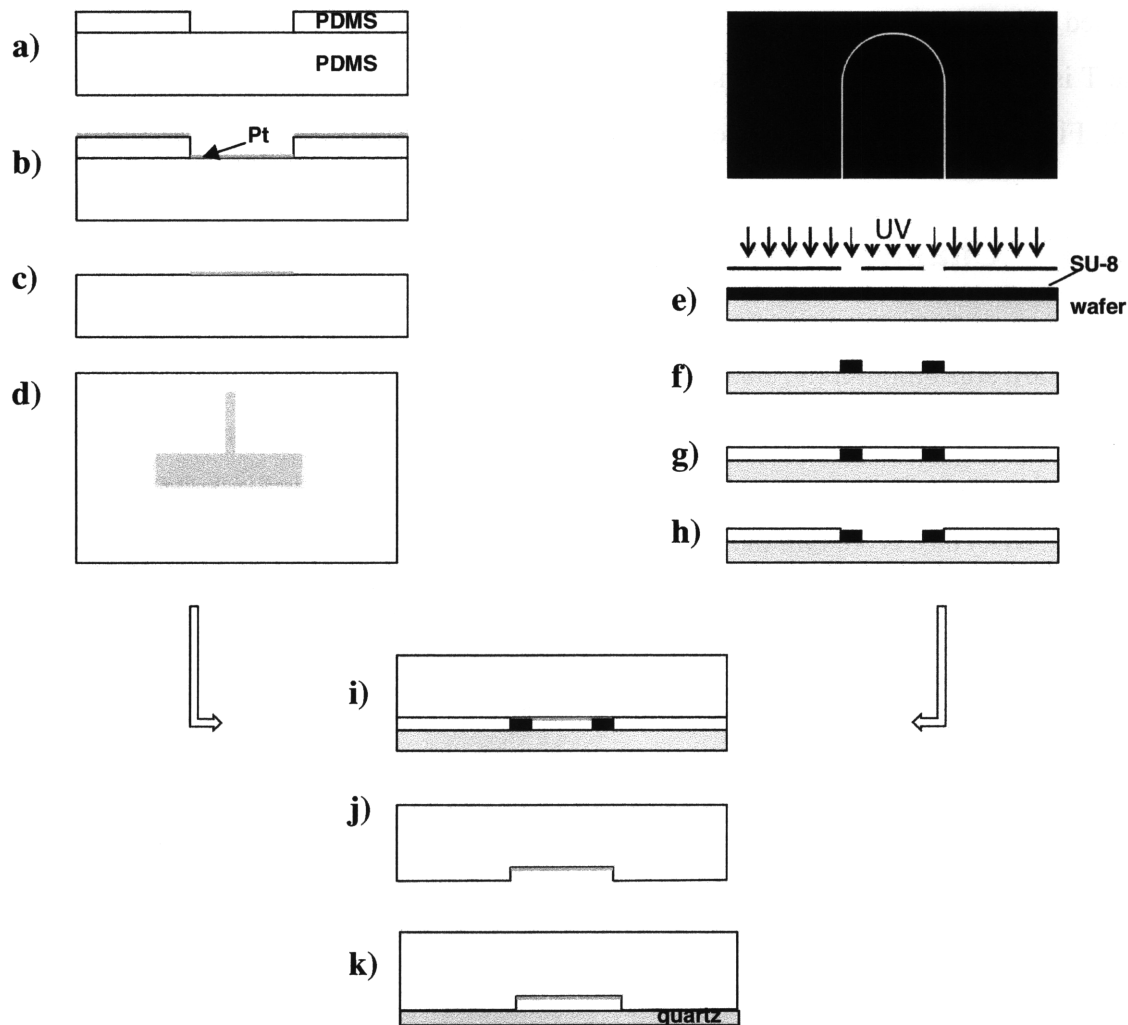
Figure 4.3: Schematic view of fabrication steps to assemble the microfluidic device. (a-d) denote the electrode fabrication; (e-h), the channel fabrication; and (i-k), device assembly.

to the cathode, a pearl of silver epoxy adhesive (MG Chemicals, BC, Canada) was placed on the leg of the T-shaped electrode before assembly. The device was baked again for 10 min at 80°C. Heparin, an anti-coagulant, was flowed through the fully assembled device and stored overnight, or until blood experiments were conducted, at room temperature.

4.2 Testing oxidative capacity

Prior to experimentation with whole blood, it was important to perform tests to qualitatively assess the oxidative capacity of the photocatalytic fluidic device. We wanted to observe the effects of various flow rates and applied bias voltages on the device's ability to oxidize water, and analyze how electrolysis may contribute to oxygen production. Because this is a device operating in real-time, the fluid flow rates are a contributing factor to how much oxygen is produced and binds to hemoglobin. The rates are inversely proportional to the residence time, or the time it takes a fluid particle to traverse the length of the fluid channel. It is clear that a longer residence time is favorable; the Peclet number in such a case is very small and there is ample time for diffusion of oxygen from the fluid/photocatalyst interface through the height of the channel. However, *in vivo*, 5 liters of blood flows through the lung every minute and to handle the large volume of blood, the device for blood oxygenation will need to operate at higher flow rates.

The purpose of the bias voltage is to enhance photocatalytic activity. Initial experiments aided in determining what the optimum bias for the operation of the microfluidic device would be. During the design stage, it was a concern that the bias would induce electrolysis of the water, such that it would not be determinable whether the blood was being oxygenated by photo-induced water splitting or electrolysis. High voltages are also a concern because of the potential damage to red blood cells and the initiation of blood clotting, due to high fluid temperatures. The following experiments were conducted in order to investigate the effect of various bias voltage.

Methylene blue (MB) is an organic dye that serves as a redox indicator and has been used in several applications to test photocatalytic activity.[35,36,37] The molecular structure of MB is shown in Figure 4.4. When in contact with the electron vacancies on the surface of UV-illuminated titanium dioxide, oxidation of the MB molecule cleaves the aromatic groups and the dye solution loses its blue color. For the experiments that are discussed as follows, the dye's degradation was quantified by performing an absorbance measurement with a spectrophotometer (SpectraMax M2^e Microplate Reader) before and after one pass through the microfluidic device, while fully operational. The MB dye (Sigma-Aldrich, 0.05 wt% in H_2O) has an absorbance is λ_{max} = 665 nm and it was diluted in DI water to an initial concentration of C_0 = 1 μM. The degradation of the dye, as determined from the spectrophotometer reading, was expressed as the ratio of final dye concentration, C, to its initial concentration, C_0.
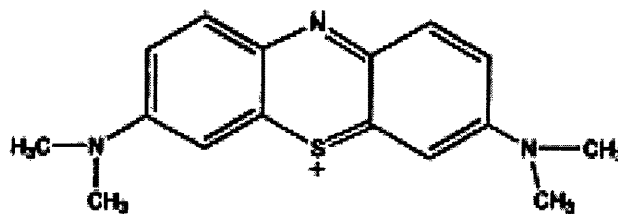
Figure 4.4: The molecular structure of methylene blue, $C_{16}H_{18}ClN_3S$. [Reproduced from Houas et al., 2007][38]

4.2.1   Bias voltage experiments

The flow of the dye solution was controlled by a Harvard Pump 11 plus syringe pump (Harvard Apparatus, Holliston, MA) and the rates were set such that the residence times for each were 7.5 s, 15 s, 30 s, 60 s, and 150 s. A microfluidic device fabricated with a 50 nm-thick TiO_2 film was illuminated with UV light (Exfo, OmniCure 2000 Series), in the manner shown in Figure 4.1A, at a distance of 8 cm from the quartz substrate. The UV spot curing system used relayed light from a UV lamp with a peak wavelength at λ = 365
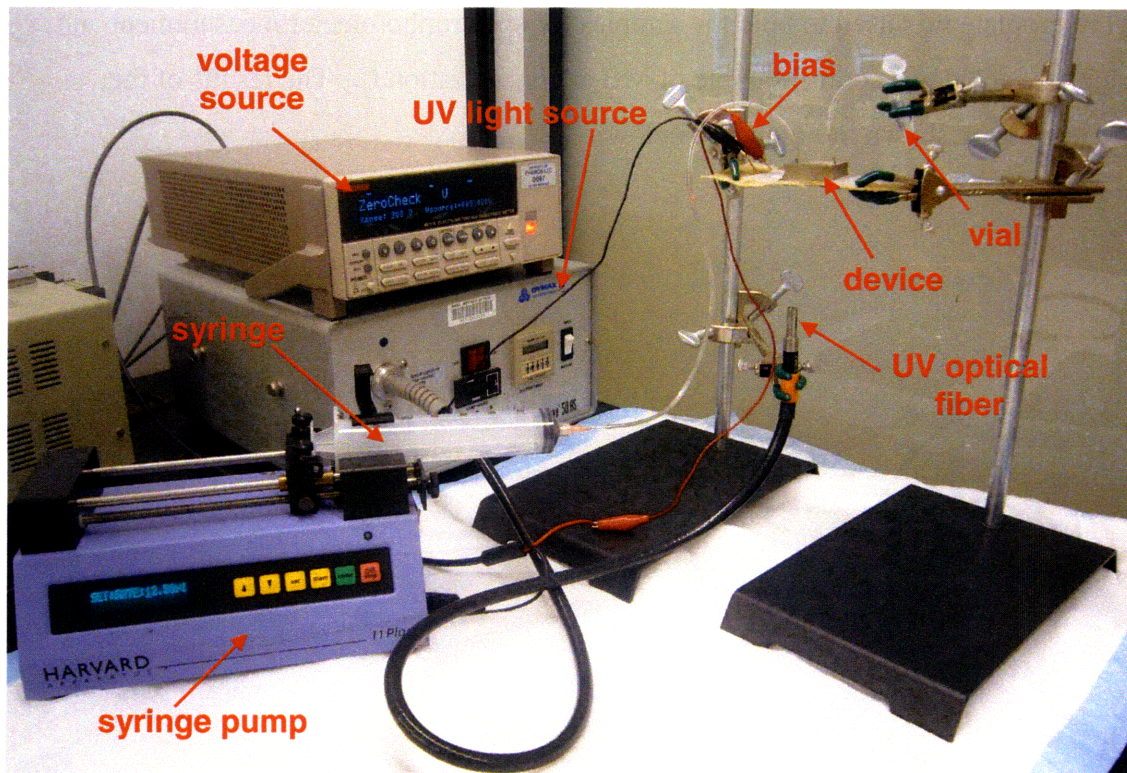
Figure 4.5: Photo of experimental set-up with UV optical fiber.

nm via a 5 mm-diameter optical fiber at an intensity measured at 7.5 W/cm^2. The bias voltage was applied between the platinum electrode and ITO using a voltage source (Model *6517A* Electrometer/High Resistance Meter, Keithley Instruments, Cleveland, OH) and was varied from no bias to 5V, in one volt increments. For a better understanding of the experimental set-up, please see Figure 4.5. A standard sterile 96-well microplate was used to hold the samples for spectrophotometer measurement and each plate included a control sample of MB at concentration C_0. The results of the experiments are shown in Figure 4.6 below.
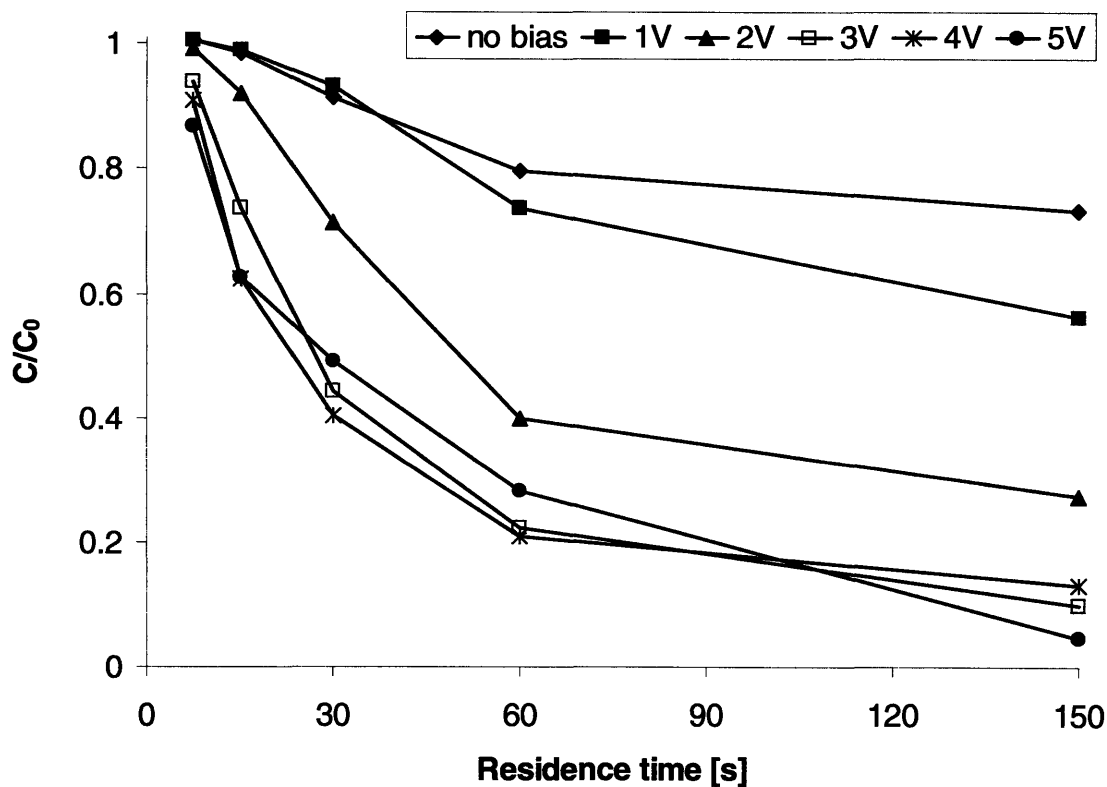
Figure 4.6: Effect of bias voltage on methylene blue degradation.

Figure 4.6 shows methylene blue degradation, represented by the concentration of MB normalized by its initial concentration, as a function of residence time. The results show that the oxidation of the dye increases the longer the residence time within the photocatalytic cell, as expected. The exponential decay of dye concentration indicates that the oxidation reaction may be of first order and can be expressed by Eq. 4.1,

$$\frac{dC}{dt} = -\kappa C$$
(Eq. 4.1)

where C is the concentration, t is residence time and κ is the first-order rate constant. κ is a function of the experimental conditions—intensity of UV illumination of the photocatalyst, photocatalyst thickness, initial dye concentration, and bias voltage. Since the UV illumination, thickness and C_0 are kept constant, κ is dependent only on the bias voltage. The data for each set of bias experiments was fit, using the method of least-squares, to the equation:

$$\frac{C}{C_0} = \exp\left(-\kappa t\right)$$
(Eq. 4.2)

Table 4.1 below shows the calculated decay rate constants and the corresponding R^2 values for the fits. The no bias case shows the degradation of the dye from the oxidizing effect of holes that have managed to migrate to the solution/photocatalyst interface without recombining with free electrons. The κ value for the device operating at 5V bias is nearly ten times that of the no bias case, demonstrating that the bias voltage can greatly enhance the photocatalytic effect. The data in Figure 4.6 and Table 4.1 also show that there is little difference between the effect of bias voltages 3V, 4V and 5V since the curves corresponding to those cases nearly lie on top of one another and the rate constants are similar in value. As a result of these experiments, the microfluidic chips from this point on were operated at 3V bias voltage.

Table 4.1: Rate constants for methylene blue degredation under various bias voltages.

Bias Voltage	Rate constant, κ [s^{-1}]	R^2 value
No bias	0.0023	0.8625
1V	0.0039	0.9564
2V	0.0096	0.8804
3V	0.0172	0.8873
4V	0.0159	0.6999
5V	0.0209	0.9941

4.2.2   Electrolysis experiments

Methylene blue is capable of degradation through direct or indirect electrolysis[36], which draws concern about the results obtained in the previous section for the bias voltage experiments. It is possible that what is presumed to be oxidation by photocatalysis is actually electrolysis—an issue that should be addressed since the same possibility exists for water in blood. The following experiments were conducted in order to show the contribution of electrolysis to methylene blue degradation.

Similar to the bias voltage experiments, MB solution at an initial concentration of C_0 was pumped through two microfluidic devices such that the residence times were 7.5 s, 15 s, 30 s, 60 s, and 150 s. The devices differed in the following manner: during the metal oxide film deposition part of chip fabrication, only ITO was deposited onto the substrate of Device 1. No TiO_2 was deposited and, as result, the only means of MB degradation would be the voltage supplied across the Pt electrode and ITO film. For Device 2, a 50 nm TiO_2 film was deposited on top of the ITO electrode. Three sets of experiments were conducted: (1) one with Device 1, with no UV illumination and operating at 1V bias; (2) another with Device 1, with no UV illumination and operating at 5V bias; and (3) one with Device 2, illuminated with UV as described previously and operating at 3V bias.
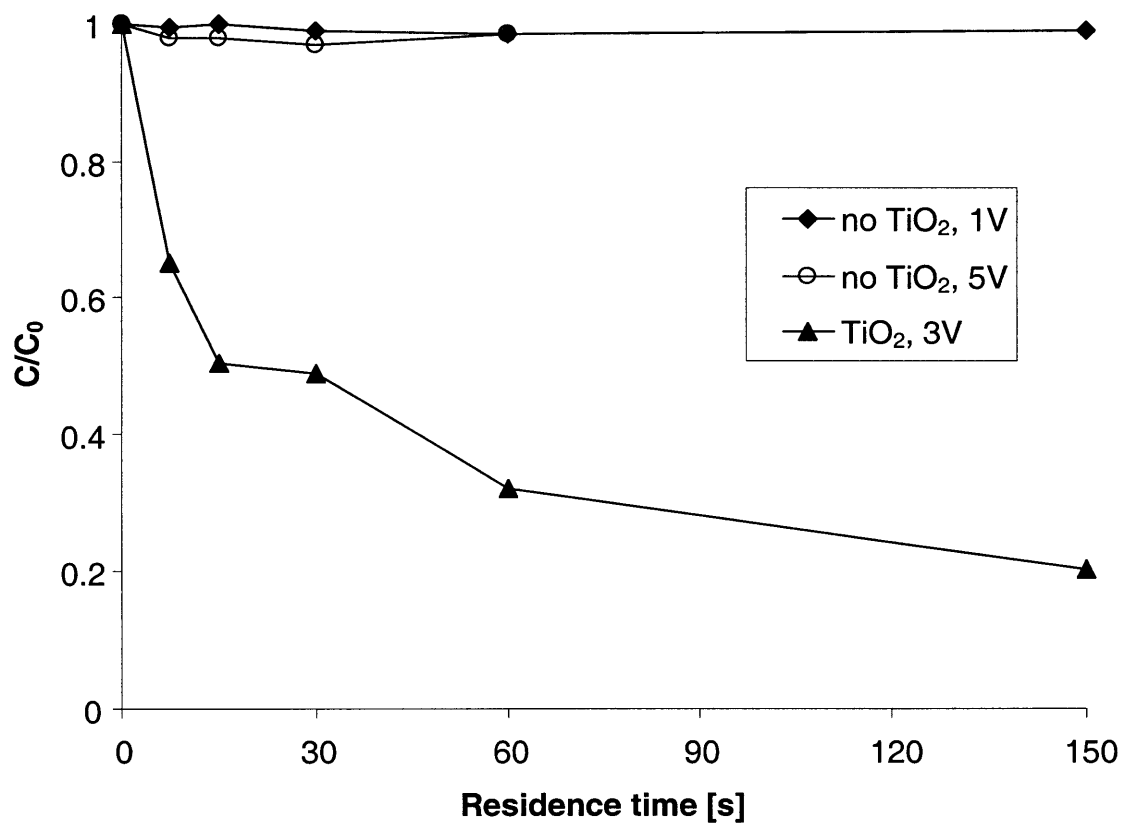
Figure 4.7: Effect of electrolysis on methylene blue degradation.

Figure 4.7 shows the data gathered from the electrolysis experiments. The normalized concentration ratio is plotted as a function of the residence time. Under 1V bias and no photocatalyst, MB shows no degradation with the concentration essentially remaining constant at C_0. Under 5V bias and no photocatalyst, there is some MB degradation, but not nearly as much as there is under the effect of photocatalysis. Upon UV illumination, the chip containing a 50 nm-thick TiO_2 film oxidizes the MB by nearly 80% during a residence time of 150 s. These results put to rest the concern that electrolysis is mistaken as photocatalysis and shows that MB degrades mostly due to the oxidation reaction.

The experimental results with methylene blue were promising. They showed that the device as designed is capable of real-time photocatalytic oxidation of the fluid flowing through it. The results provided us with a means of judging how best to operate the device to achieve optimal electron-hole production (i.e. determining the optimum bias voltage). The next, and vital step, is to demonstrate that blood oxygenation is possible with the microfluidic device.

4.3 Blood oxygenation

Bovine blood obtained from a slaughterhouse (Blood Farm, Groton, MA) was used for blood oxygenation experiments. The blood was about 36 hours old and treated as follows: a solution of 20,000 units heparin in 40 ml sterile Dextrose (5%) was added to approximately 200 ml of blood obtained from a single cow. The blood was then gently stirred to incorporate the heparin into the fresh blood. This was done to guarantee an activated clotting time (ACT) of approximately 400 seconds at room temperature, an accepted value for a cardiopulmonary bypass procedure,[39] and minimize blood clotting within the microfluidic device.

The device was also prepared to safeguard against clotting by flowing heparin through its channels and storing the device in room temperature overnight. It was determined necessary to follow this procedure especially for freshly fabricated devices, otherwise protein adhesion would result immediately after blood started flowing through the

channel. The plastic tubing (Masterflex® Tygon® tubing, Cole-Palmer) and the syringe (60 mL Louer-Lok, BD) used to pump the blood through the chip were biocompatible; the tubing connecting pins (18 gauge, New England Small Tube) were not so they were stored in heparin and changed frequently between experiments.

After the blood and device preparation, the experiments were performed as follows: a syringe was filled with approximately 25 mL of heparinized whole blood and tested using a commercial blood gas analyzer (ABL 520, Radiometer, Denmark) to determine hemoglobin saturation level (sO_2 [%]), pH, carbon dioxide partial pressure (pCO_2 [mmHg]), oxygen partial pressure (pO_2 [mmHg]) and hemoglobin count (tHb [g/dL]). The pH and pCO_2 were measured for monitoring purposes, but the other measurements were made in order to calculate the oxygen content, CaO_2, in blood using the Fick principle:

$$CaO_2 = \alpha \cdot tHb \cdot \left(\frac{sO_2}{100}\right) + \beta \cdot pO_2 \qquad \text{(Eq. 4.3)}$$

where CaO_2 is calculated in units of [mL O_2/ 100 mL blood], α is the binding capability of oxygen to hemoglobin (1.34 mL O_2/ g Hb) and β is the solubility of oxygen in blood (0.0031 mL O_2/ (100 mL blood · mm Hg)). The first term on the right hand side of Eq. 4.3 represents the oxygen bound to hemoglobin while the second term is the amount of oxygen in solution. Preliminary experiments show that volume of dissolved gas in blood plasma constitutes approximately one percent of the total oxygen content.

The blood was then pumped through the microfluidic device at a flow rate of 12.5 μL/min, corresponding to a residence time of 54 seconds. The experimental set-up was the same as it was with the methylene blue experiments (see Figure 4.5). The UV spot curing system illuminated the device from underneath at a distance of 8 mm from the quartz substrate. The discharge tubing was submerged in a vial filled with ~300 μL paraffin oil (OVOIL™, Vitrolife, Sweden) and $n = 3$ samples (100 μL each) were collected. The oil served as a barrier between the blood and the environment to prevent

further oxygenation once the fluid flowed out of the device. The samples were then tested by the blood gas analyzer once again to determine the oxygen content at the exit.

4.3.1   Blood oxygenation experiments

The goal of the first set of experiments was to observe the effect of the initial oxygen saturation, sO_2 [%], of the blood on its change in calculated oxygen content, CaO_2, after one pass through the microfluidic device. The sO_2 is the percentage of red blood cell hemoglobin that has oxygen bound to it. The hypothesis is that the CaO_2 should remain the same regardless of the initial value of sO_2; the production of oxygen from the photocatalyst surface should remain constant with the same blood flow rate through the device, UV illumination, and TiO_2 film thickness. In the case of the following experiments, the flow rate was maintained at 12.5 μL/min and the TiO_2 thickness was 50 nm.

The sO_2 was varied by aspirating the syringe containing the blood after each experiment and allowing the fluid to exchange gases with the ambient air for five minutes. The sO_2 values were S1 = 23.6%, S2 = 34.4%, S3 = 45.0%, S4 = 64.0%, and S5 = 75.7%. The results of the experiments are shown in Figure 4.8 below.
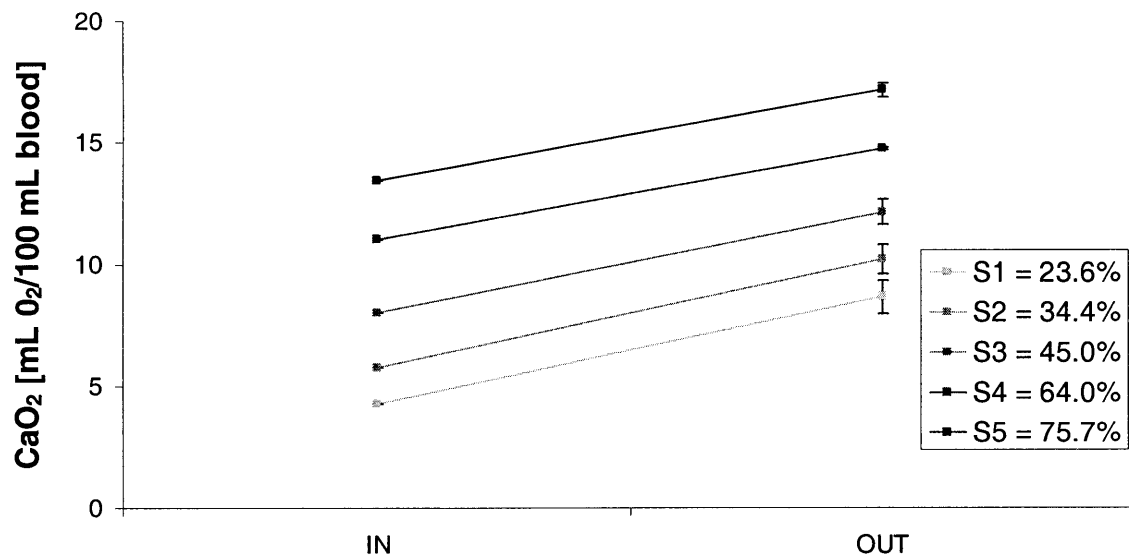
Figure 4.8: Increase in blood oxygen content for various initial O_2 saturation.

These preliminary results show that the microfluidic device used increased the blood oxygen content by an average of 4.06 ± 0.32 mL $O_2/100$ mL blood. As presumed earlier, the initial saturation had little effect on the amount of oxygen binding to hemoglobin and in solution, and the change in CaO_2 value was approximately constant. In Chapter 2, it was stated that in the lung the increase of oxygen is 6.5 mL $O_2/100$ mL blood. With the proof-of-concept microfluidic device, as it was designed, it is possible for us to oxygenate blood two-thirds the amount the lung does. Also mentioned in Chapter 2 was the fact that, *in vivo*, venous blood enters the lung at a sO_2 level of 64% and leaves at 96%. In our experiments, sample S4 entered at 64.0% and exited the device at an average sO_2 value of 85.6%. Sample S5 entered at 75.7% and exited the device at an average sO_2 value of 96.6%. Results are quite close to the *in vivo* values. Granted, the microfluidic device is operating at a flow rate much slower than that of the blood flow in the lung (5 L/min), but these are a very promising result nonetheless. With further improvements to the device, it may be possible to fully oxygenate venous blood as the lung does and ultimately to also handle the blood volume that the lung does.

To provide some prospective on the results, Table 4.2 lists the oxygen producing capacity of other photocatalytic fluidic devices for artificial respiration. Subrahmanyam *et al* have a photocatalytic cell (PC) that does not oxygenate blood in real-time and produces 2.41 x 10^{-5} mmol O_2/(cm^2 · min).[34] Our colleagues, Gilbert *et al* created a real-time fluidic PC and produced nearly triple that amount, 6.25 x 10^{-5} mmol O_2/(cm^2 · min).[31] Neither device was a microfluidic device or had channel heights as small as ours (100 μm).The microfluidic device for blood oxygenation produced an oxygen flux of 1.11 x 10^{-3} mmol O_2/(cm^2 · min), two orders of magnitude larger than any other PC to date.

Table 4.2: Comparison of oxygen flux from different PC designs.

	Subrahmanyam *et al, 2007*	Gilbert *et al, 2007*	Our results
photocatalytic cell volume [cm^3]	10	5.5	0.01125
photocatalyst surface area [cm^2]	14.32	9.6	1.125
CaO$_2$ [mL O$_2$/ 100 mL blood]	10.13	N/A	4.06
$\dot{V}''$ **[mL O$_2$/ (cm^2 · min)]**	5.90 x 10^{-4}	N/A	2.71 x 10^{-2}
$\dot{n}''$ **[mmol O$_2$/ (cm^2 · min)]**	2.41 x 10^{-5}	6.25 x 10^{-5}	1.11 x 10^{-3}

4.3.2   Experimental observations and issues

The first round of experiments was successful in demonstrating that the microfluidic chip works; however, there were several experimental issues encountered and observations made that ought to be discussed.

First, there was a concern that the photo-induced oxidation reaction would lower the pH of the blood because of hydrogen ion evolution. This is a legitimate concern as the pH in the body affects the function of various proteins and critical reactions. It was expected, however, that the buffering capacity of the blood would maintain the pH at physiological level, 7.4. Carbonic acid is the body's means of regulating the pH and its dissociation is given by the Henderson-Hasselbalch equation:

$$H_2 CO_3 \leftrightarrow H^+ + HCO_3^-$$
(Eq. 4.4)

The experimental results validated the assumption. It was observed that average pH values between inlet and outlet were nearly the same, 7.19 and 7.25, respectively. The minor difference lies within one standard deviation and it was demonstrated that the blood pH was not adversely affected by the photocatalytic effect.

The second observation, and one not so easily dismissed, was that the light intensity reaching the photocatalytic film was perhaps a lot more than was needed for oxidative holes to form. As mentioned earlier, the UV optical fiber emitted light at an intensity of 7.5 W/cm^2 and, assuming no loss, the intensity of light reaching the surface of the device was 2 W/cm^2. The film is essentially blasted with UV light. The devices that were fabricated for blood experiments generally had a lifetime of four experiments before they could no longer be used. Protein adhesion on the TiO_2 contributed significantly to the short lifetime of the devices. Protein adhesion and blood clotting occluded the channels to the point where the hydraulic resistance prevented the flow of blood. Furthermore, adhesion decreased the effective surface area of the photocatalyst. Flowing heparin through the device between experiments made negligible difference once the adhesion

had already taken place. The hypothesis was that the intensity of light was so high that the fluid temperature rose and thus encouraged cell and protein adhesion, an issue plaguing many biomedical devices.

A new UV light emitting device was designed so that the intensity would be tunable and there would be minimal heat generation. Yang-Hyo Kim, a student in the Department of Mechanical Engineering, made a light guide that would relay UV light (λ= 365 nm) via three LEDs directly to the area where the photocatalyst was deposited onto the quartz substrate. Figure 4.9 is an annotated photo of the light guide. The LEDs were placed under a diffuser to ensure that the light reached the device with uniform intensity. A sink was placed underneath because the electrical components generated heat. The light guide was connected to a DC power supply (Tenma, Model 72-6610) and the intensity of the UV LEDs varied linearly with the supplied current. For all the experiments following this point, the microfluidic device was directly attached to the light guide and the UV spot curing system was no longer used. The change decreased the incidence of protein adhesion and improved the lifetime of the devices.
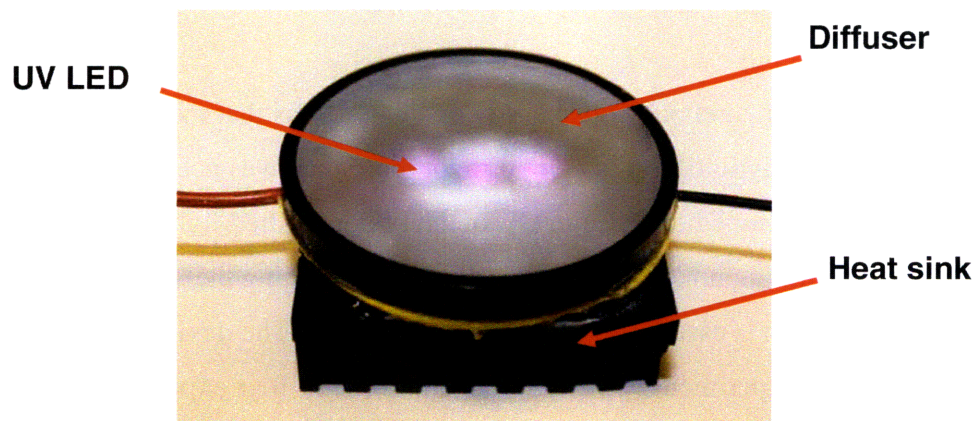

Figure 4.9: UV light guide

4.3.3 UV light intensity experiments

The new UV light guide allowed a round of experiments that aided in determining the minimum UV light intensity required to operate the microfluidic chip. The experimental set-up is shown in Figure 4.10 (the voltage and current sources are not shown). Blood, at an initial saturation of approximately 17%, flowed through a chip fabricated with a 50 nm-thick TiO_2 film at a rate of 12.5 µL/min. The blood was tested by the blood gas analyzer before and after one pass through the device. Three samples of blood were collected in vials of oil, as was done previously. The UV light intensity was varied (by changing the current to the guide) from 10 mW/cm^2 to 90 mW/cm^2, in increments of 10 mW/cm^2 for each data point. Figure 4.11 provides the results.
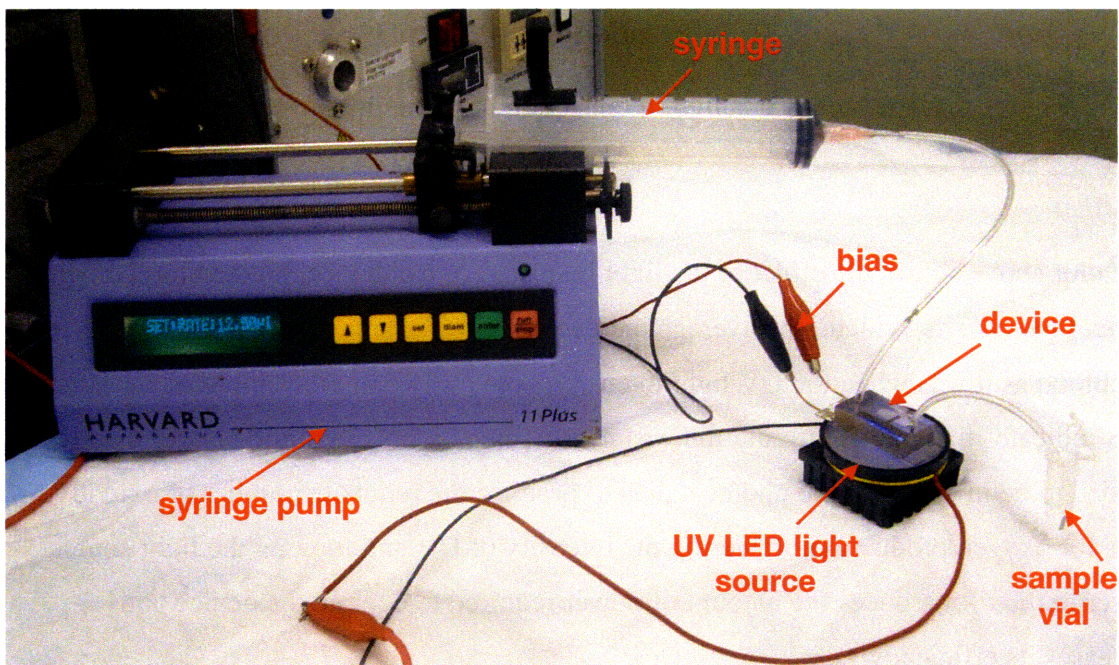
Figure 4.10: Photo of experimental set-up with UV LED.
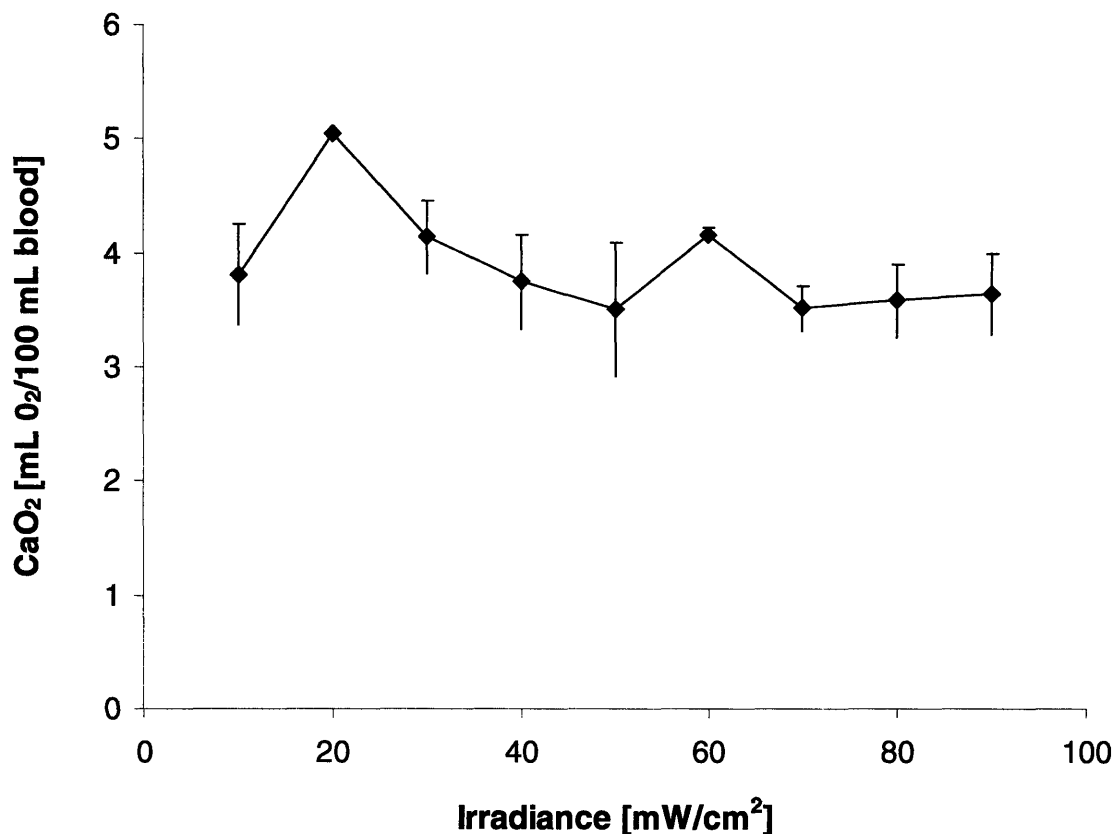
Figure 4.11: Effect of UV light intensity on increase in blood oxygen level.

The plot above shows the effect of the light intensity, or irradiance, on the blood oxygen content gain. As is evident, the average increase in CaO_2 is approximately 4 mL O_2/ 100 mL blood as it was when the UV light intensity 8 cm away from the chip was 7.5 W/cm². This indicates that the UV irradiation was nearly three orders magnitude larger than it needed to be in order for the photocatalyst to produce the requisite number of oxidative sites for oxygen production. Lowering the intensity of UV and moving the light source closer to the film reduces the amount of power required to operate the device and increases its efficiency.

The data also suggests that an irradiance of 20 mW/cm² is the optimum for oxygen production for this device. The CaO_2 increase at this UV intensity is 5.05 mL O_2/ 100 mL blood, approximately 1 mL O_2/ 100 mL blood over the average. The reasons why the

maximum occurs at this intensity is not known. However, the experiments following proceed with the UV light intensity maintained at 20 mW/cm^2.

4.3.4   Film thickness experiments

The goal is to increase the oxygen output from the thin film photocatalyst and oxygenate blood to the degree that it is done in the lung. TiO_2 thickness was assessed to determine whether a thicker film, when irradiated by UV, would generate more electron-holes and have a greater oxidative capacity. The following experiments involved five devices in which the TiO_2 thicknesses were 50 nm, 100 nm, 150 nm, 300 nm and 400 nm. The UV light intensity was 20 mW/cm^2 and the initial oxygen saturation level was approximately 30%. Similar to the experimental protocol for the methylene blue experiments, the flow rates were varied to plot the increase in CaO_2 as a function of the residence time of blood in the cell. The flow rates were 100 μL/min, 50 μL/min, 25 μL/min, 12.5 μL/min and 6.25 μL/min corresponding to residence times of 6.75 s, 13.5 s, 27 s, 54 s and 108 s, respectively. To obtain more accurate results, the blood collected after one pass through the device provided a sample size of $n = 10$. As always, the samples were tested using the blood gas analyzer and the increase in CaO_2 was calculated from the data collected.
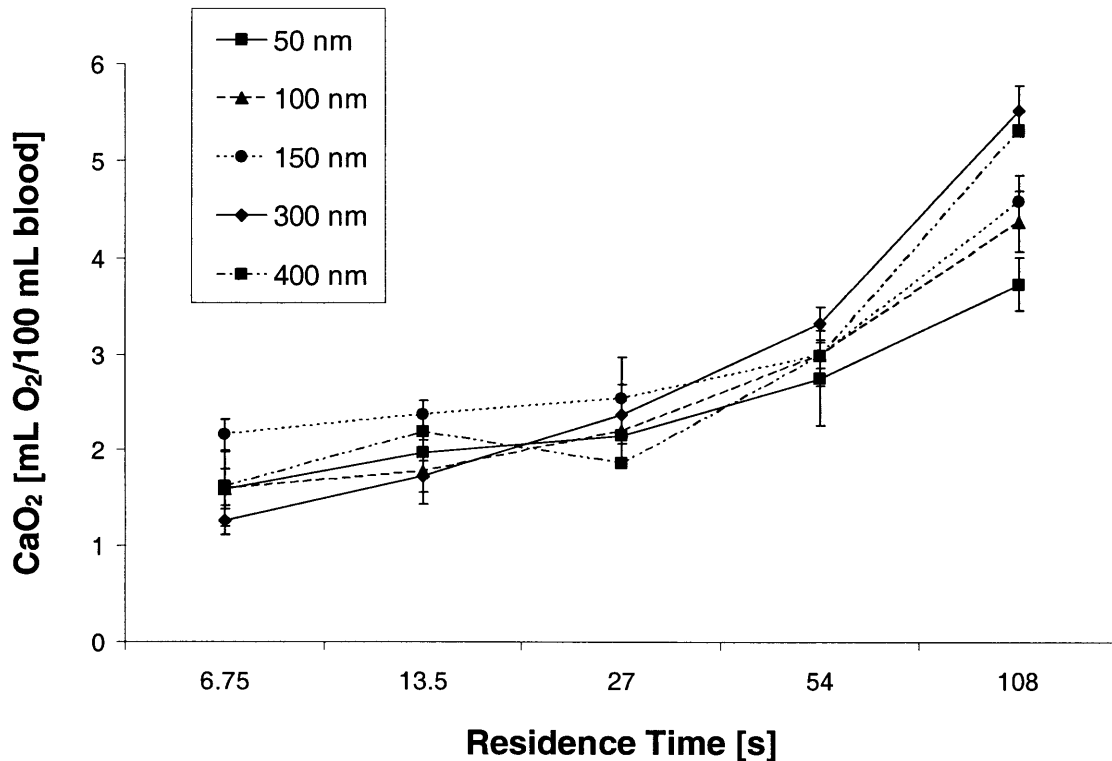
Figure 4.12: Effect of titanium dioxide film thickness on blood oxygenation.

Figure 4.12 displays the results obtained from the experiments outlined above. As one would expect, the longer the residence time within the device the greater the increase in the blood's oxygen content. All five films oxygenated blood to similar levels at low residence times (high flow rates) but as the residence times increased the plots diverged to indicate a marked difference between the oxygen outputs of the TiO_2 films. As expected the dissolved oxygen production increased with thickness, with the 50 nm film performing the poorest and the 300 nm performing the best, producing an average of 3.73 mL O_2/ 100 mL blood and 5.52 mL O_2/ 100 mL blood, respectively, at a residence time of 108 s. Interestingly, the 400 nm film produced 5.31 mL O_2/ 100 mL blood for the same residence time, within one standard deviation of the 300 nm value.

The lack of improvement despite the 100 nm increase in TiO_2 thickness could be an indication that a thickness of 300 nm thickness yields a limit to the oxygen production of

the TiO_2 film. In fact, it has been proposed that the optimum thickness for a titanium dioxide thin film is on the order of the wavelength of UV light, 365 nm.[14,18] The exact reasons are unknown at present. Considering the results obtained and represented in Figure 4.12, it is plausible. As a result, it is recommended to use a TiO_2 film thickness of approximately 350 nm for future devices.

4.4 Conclusions

This chapter covered the design of the microfluidic device for artificial respiration and the experimentation that was done to validate its function. The results presented have shown that although the device cannot produce, as of yet, the amount of oxygen that is transferred to the lung *in vivo*, it is capable of producing 4.06 mL O_2/ 100 mL blood with a 50 nm TiO_2 film and a flow rate of 12.5 μL/min. The increase in oxygen content is almost two-thirds of that which is transferred in the lung, 6.5 mL O_2/ 100 mL blood. We have also achieved a maximum CaO_2 value of 5.52 mL O_2/ 100 mL blood with a device fabricated with a 300 nm film and blood flowing at a rate of 6.25 μL/min. In the process of conducting these experiments, we have also determined the optimum conditions under which to operate the microfluidic device—a bias voltage of 3 V and illumination of TiO_2 with 20 mW/cm^2 UV light. The results for the single-layer microfluidic device are an excellent starting ground for a second generation device that could be capable of sustaining the respiration of a small animal or, perhaps, even a human.

(This page intentionally left blank)

Chapter 5

Summary and Future work

The sobering statistics on the prevalence of lung disease and the lack of appropriate therapies for sufferers of acute and chronic symptoms encouraged the development of a microfluidic device for artificial respiration. This thesis discusses a bulk of the research that was conducted in order to produce a device with a high yield of dissolved oxygen gas through photocatalytic water splitting and to validate its capability to oxygenate whole bovine blood. The artificial respiration project lies at the intersection of several engineering disciplines – materials science, nanoengineering, fluid mechanics, mass transfer and optics, to name a few – and, therefore, there are many directions that could be taken to explore how best to create an efficient photocatalytic lung replacement.

The goals outlined in the introduction are to (1) optimize the function of the thin film photocatalyst so that it can produce enough oxidative sites for oxygen production and (2) integrate the photocatalyst and microfluidics components seemlessly to create a device for real-time blood oxygenation. In Chapter 3, the various methods of titanium dioxide deposition, and their advantages and disadvantages, were discussed. Two methods for thin metal oxide film fabrication, sol-gel and reactive D.C. magnetron sputtering, were chosen to perform experiments to determine which method and what type of protocol will yield highly crystalline and smooth films. Reactive sputtering was found to produce robust and crystalline anatase films that promise high photocatalytic activity.

In Chapter 4, the design of a complete microfluidic device incorporating the photocatalyst was discussed. The challenges in fabricating the device stemmed from having to create a microfluidic chip that was an analogue of an electrochemical cell. The photocatalytic cell (PC) contained a fluid channel, a Pt electrode that served as the

cathode and ITO/ TiO_2 junction that served as the anode. Standard microfabrication techniques were used and some new techniques were developed to realize the design that was proposed. To validate the function of the PC, a redox indicator, methylene blue (MB), was initially used. In later experiments, however, bovine blood was used as the oxygen carrier and the oxygen producing capability of the devices were assessed.

The results are very promising. Preliminary blood oxygenation tests show that a chip fabricated with a 50 nm-thick titanium dioxide film and with blood flowing through it at a rate of 12.5 μL/min produces an average of 4.06 mL of oxygen per 100 mL of blood. That translates to an oxygen flux of 1.11 x 10^{-3} mmol O_2/ (cm^2 · min), more than two orders of magnitude larger than that of any other fluidic device for artificial respiration to date. Further experiments show that it is also possible to produce up to 5.52 mL O_2/ 100 mL blood in a device with a 300 nm film. That nearly reaches the value of 6.5 mL O_2/ 100 mL blood, which is the oxygen transfer that occurs in the lung.

Before implanting the device into a patient with lung disease, there are a few things to consider. The blood flowing through the human lung is pumped by the heart at a rate of five liters per minute. In order to oxygenate venous blood after it enters the lung to oxygen saturation levels of arterial blood, oxygen from the environment must diffuse through three million alveoli at a rate of 313 mL/ min. Since the rate of bovine blood through the microfluidic device is fairly low (12.5 μL/min), the chip with 50 nm of TiO_2 produces only 3.05 x 10^{-2} mL O_2 per minute. If this device where to sustain human life, it would need to be approximately one square meter. Therefore, there is still a good deal of work to be done to move towards implanting a microfluidic blood oxygenator into a human patient.

Future steps to improve the device's function must include the development of a multilayer device to accommodate the large pulmonary blood flow rate and to provide the surface area necessary to produce the requisite volume of oxygen. Currently, a two-layer microfluidic device is being developed in the hope that the design concept can be extended to a device of n layers. The main design challenge is the following:

Each fluidic layer of the device is independent from the other. Each channel must have access to a thin film photocatalyst for oxygen production and that means that UV light must be relayed to each photocatalyst layer. A UV light guide, made of a thin (~0.5 mm) plate of quartz or some type of polymer, that can be illuminated from its edge and emit light from its two planar faces is proposed to irradiate the thin titanium dioxide films for electron-hole production. It is also desired to sputter the ITO and TiO_2 films directly onto this light guide; therefore, the materials used ought to be easily fabricated and inexpensive as they will be disposable. If there are n layers, then an array of ½ n light guides are required. A means of relaying UV light to each one from an external source is also required. Distancing the source is desirable because any heat generating electrical elements will not be in close contact with the blood. However, there will be issues due to the intensity loss from total internal refraction. The development of the optics component alone is complex enough to warrant a separate design project.

There are limits to how effectively a single-layer device can function. If an implantable, self-contained real-time blood oxygenator is the objective, a multi-layer device is essential. A multi-layer device will increase the photocatalyst surface area to device volume ratio, driving its efficiency closer to that of a real lung. Although the artificial respiration project is far from complete, the work that is presented in this thesis is a stepping stone towards the realization of a lung replacement. The microfluidic device for blood oxygenation will ultimately have a huge impact in the fields of bioengineering and bioMEMS, microfluidics and medicine.

(This page intentionally left blank)

Appendix A

Microfluidic device fabrication

A.1   ITO/TiO$_2$ thin film deposition

The ITO and TiO$_2$ films were patterned onto quartz glass wafers (3" diameter and 700 μm thick) and the wafers were cut into slides to produce individual substrates for the microfluidic devices. The following is a detailed protocol of the fabrication.

Each quartz wafer (Mark Optics Inc., Santa Ana, CA) was cleaned using a three-step solvent rinse, first with acetone, followed by methanol and then with isopropanol. The wafers were dried with nitrogen and baked at 150°C in order to eliminate any residual solvents. AZ-4620 positive photoresist (Shipley, Corp., Somerville, NJ) was spun onto the clean wafer at a rate of 1500 rpm for 60 s to obtain a thickness of 10 μm. The wafer was then placed for one hour in a 90°C oven, along with a dish of water to maintain a humid environment inside the oven. This was done to prevent the resist from drying out.

Photolithography was performed using a dark-field high resolution transparency mask, printed at 3550 dpi (Mikacolor, CA). The mask is shown in Figure A.1. After the bake, the wafer was exposed through the transparency with the MJB3 Broadband Mask Aligner (Karl Suss, VT) with an exposure rate of approximately 3 mW/ cm^2 for 36 s. The wafer was then placed in a dish of MIF440 developer for 5 min, gently agitated, and then rinsed with DI water. The quartz was masked with photoresist except for the areas where the ITO and TiO$_2$ were to be deposited, as shown in Figure A.1.
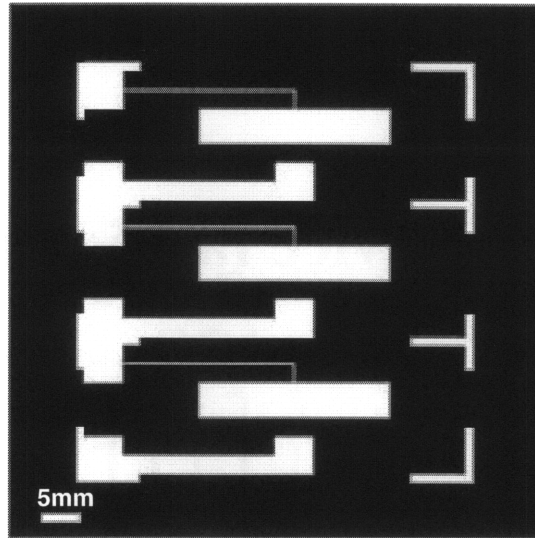
Figure A.1: Transparency mask for quartz substrate.

The sputtering protocol is as follows: The wafer was placed in the deposition chamber of the Orion 5 high-vacuum sputtering system (AJA International, Inc., N. Scituate, MA) and the chamber was pumped down using a turbopump operating at 1000 Hz. Argon gas was introduced into the chamber at 12 sccm and the deposition pressure was set to 3 mTorr. The plasma around an ITO target, powered with an RF gun running at 215 W, was ignited. A 30 min run deposited approximately 200 nm of ITO onto the substrate. After removing the wafer from the sputtering chamber, the areas where ITO needed to be exposed to make electrical connections were masked by manually swabbing AZ-4620 onto those areas. The wafer was baked again at 90°C.

Titanium dioxide was deposited on top of the ITO using the protocol developed in Chapter 3: the wafer is placed in the sputtering unit, O_2 gas at 1.8 sccm and Ar gas at 10.2 sccm flowed into the chamber, and the deposition pressure was set to 3.6 mTorr. The Ti target powered by the DC magnetron gun ran at 250 W. The reactive sputtering deposition rate was roughly around 1.5 Å/s. The thickness of TiO_2 was varied and thus the deposition times varied.

After the second round of sputtering, the wafer was placed in an acetone bath and cleaned in an ultrasonicator for 5 min. At that point, the resist was removed to reveal ITO and TiO_2 in the desired patterns (see Figure 4.2). The wafer was annealed in an annealing furnace at 450°C for 1 hour and it was diced to produce three identical substrate slides 18 mm in width and 54 mm in length.

A.2   Electrode deposition

The masking of the thick PDMS pieces that constituted the electrodes was covered in Chapter 4. The deposition of the thin metal films was carried out as follows: The PDMS substrates were placed in the deposition chamber of the Orion 5 sputtering unit equipped with pure Ti and Pt metal targets (2 in diameter, purity 99.9%). The chamber pressure was maintained at 3 mTorr and Ar gas flowed through at a rate of 12 sccm. The Ti target was powered by a DC gun at 250 W and a 30 nm film was deposited onto the PDMS at a rate of 0.8 Å/s. The DC gun was then powered down and the plasma was reignited around the Pt target. It was powered by an RF gun at 215 W and a 320 nm thin film of Pt was deposited at a rate of 2.8 Å/s. The substrates were then removed from the sputtering unit and unmasked.

A.3   Channel fabrication

The channels were fabricated using soft lithography techniques. The molds were made by producing the outlines of the channel in positive relief in SU-8 50 (Microchem) on 3" Si wafers (Silicon Quest). Each silicon wafer was cleaned with solvents (acetone, methanol, and isopropanol), dried with nitrogen, and baked at 150°C on a hotplate to evaporate any residual solvents. SU-8 50 was spun onto the wafer rotating at 1000 rpm to obtain a resist thickness of 100 μm. A pre-bake of 10 min on 65°C hotplate and 30 min on a 95°C was required. Figure A.2 shows the portion of the mask that is the negative of what appears on the wafer. The channel is rectangular (4.5 mm (w) and 25 mm (l)) except that there are tapered extensions on either end of the channel. These were added into the channel for

the inlet and outlet in order to allow for developing flow and to minimize sudden expansions or contractions in cross-sectional area. The wafer was then exposed for four minutes by the MJB3 Broadband through the mask, which contained outlines for two channels. A post-bake of 1 min at 65°C and 10 min at 95°C further cross-linked the exposed SU-8. The wafer was then developed by means of an acetone spray. The mold was complete.

As mentioned in Chapter 4, the channel that is fabricated is actually a "gasket" that will lie between the PDMS with the deposited electrode. Therefore, PDMS (Sylgard 184, Dow Corning) mixed to an elastomer to curing agent ratio of 10:1 was spun onto the mold to a thickness of 100 μm, the channel height. After baking for 2 hours at 80°C, the PDMS in the region within the channel was peeled away. Thus, the channel in gasket form was fabricated.
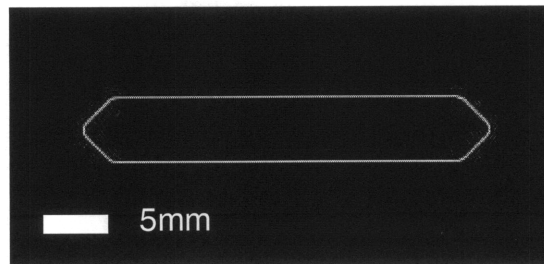
Figure A.2: Transparency mask for channel.

References

[1]   American Lung Association, "Data and Statistics," accessed Feb. 7 2009, <http://www.lungusa.org/site/c.dvLUK9O0E/b.33347/k.AC09/Data_Statistics.ht m>.

[2]   National Heart Lung and Blood Institute, "What is Chronic Obstructive Pulmonary Disease (COPD)?," accessed Feb. 7 2009, <http://www.nhlbi.nih.gov/health/dci/Diseases/Copd/Copd_WhatIs.html>.

[3]   M.M. Hoeper and T. Welte, *Eur. Respir. J.*, 2008, **32**, 1431–1432.

[4]   A. Vollmer, "Development of an Integrated Microfluidic Platform for Oxygen Sensing and Delivery," *SM Thesis*, Massachusetts Institute of Technology, 2005.

[5]   US Transplant: Scientific Registry of Transplant Recipients, "OPTN/SRTR 2007 Annual Report," accessed Feb. 9, 2009, <http://www.ustransplant.org/annual_reports/current/>.

[6]   COPD International, "Lung Transplant – General Information," accessed Feb. 9, 2009, < http://www.copd-international.com/library/lungtx_info.htm>.

[7]   R.J. Gilbert, H. Park, M. Rasponi, A. Redaelli, B. Gellman, K.A. Dasse, T. Thorsen, *ASAIO Journal*, 2007, **53**, 447-455.

[8]   A.H. Mines. *Respiratory Physiology*. 1986. Raven Press, NY New York.

[9]   J.B. West. *Respiratory Physiology: The Essentials*. 2000. Lippincott Williams & Wilkins, Baltimore, MD.

[10]   M.F. Perutz, M.G. Rossman, A.F. Cullis, H. Muirhead, G. Will and A.C.T. North, *Nature*, 1960, **185**, 416-422.

[11]   J.C. Kendrew, R.E. Dickerson, B.E. Strandberg, R.G. Hart, D.R. Davies, D.C. Phillips and V.C. Shore. *Nature*, 1960, **185**, 422-427.

[12]   A.L. Lehninger, *Lehninger Principles of Biochemistry*, W.H. Freeman & Co, New York, 2005.

[13]   A. Fujishima and K. Honda, *Nature*, 1972, **238**, 37-38.

[14]   A. Mills and S. Le Hunte, *Journal of Photochemistry and Photobiology A: Chemistry*, 1997, **108**, 1-35.

[15]   US Department of Energy, Energy Information Administration, "World
       Consumption of Primary Energy by Energy Type and Selected Country Groups,
       1980-2004,"accessed Mar. 2, 2009,
       <http://www.eia.doe.gov/pub/international/iealf/table18.xls>.

[16]   M. Kaneko and I. Okura (eds.), *Photocatalysis: Science and Technology*,
       Springer-Verlag, New York, 2002.

[17]   B. Ohtani and S.I. Nishimoto, *Journal of Physical Chemistry*, 1993, **97**, 920-926.

[18]   M. Anpo and M. Takeuchi, *Journal of Catalysis*, 2003, **216e**, 505-516.

[19]   H. Kominami, J. Kato, S. Murakami, Y. Ishii, M. Kohno, K.Yabutani, T.
       Yamamoto, Y. Kera, M. Inoue, T. Inui and B. Ohtani, *Catalysis Today*, 2003, **84**,
       181–189.

[20]   H. Kominami, S. Murakami, Y. Kera and B. Ohtani, *Catalysis Letters*, 1998, **56**,
       125–129.

[21]   R. Asahi, T. Morikawa, T. Ohwaki, K. Aoki and Y. Taga, *Science*, 2001, **293**,
       269-271.

[22]   A. Fujishima. *Journal of Photochemistry and Photobiology C: Photochemistry
       Reviews*, 2000, **1**, 1-21.

[23]   M.R. Hoffmann, S.T. Martin, W. Choi and D.W. Bahnemann, *Chemical Reviews*,
       1995, **95**, 69-96.

[24]   The New York Times, "Smog-Eating Cement," accessed Mar. 1, 2009,
       <http://www.nytimes.com/2007/12/09/magazine/09smogeatingcement.html>.

[25]   T. Watanabe, A. Nakajima, R. Wang, M. Minabe, S. Koizumi, A. Fujishima and
       K. Hashimoto, *Thin Solid Films*, 1999, **351**, 260-263.

[26]   A. Fujishima, R.X. Cai, J. Otsuki, K. Hashimoto, K. Itoh, T. Yamashita and Y.
       Kubota, *Electrochimica acta*, 1993, **38**, 153-157.

[27]   Y. Matsumoto, M. Murakami, T. Shono, T. Hasegawa, T. Fukumura, M.
       Kawasaki, P. Ahmet, T. Chikyow, S. Koshihara, H. Koinuma, *Science*, 2001, **291**,
       854-856.

[28]   P. Innocenzi, Y.L. Zub and V.G. Kessler, *Sol-Gel Methods for Materials
       Processing*, Springer Science + Business Media, the Netherlands, 2008.

[29]   Q. Fan, B. McQuillin, A.K. Ray, M.L. Turner and A.B. Seddon, *Journal of
       Physics D: Applied Physics*, 2000, **33**, 2683–2686.

[30]   P. Löbl, M. Huppertz and D. Mergel, *Thin Solid Films*, 1994, **251**, 72-79.

[31]   R. J. Gilbert, L. M. Carleton, K. A. Dasse, P. M. Martin, R. E. Williford and B. F. Monzyk, *Journal of Applied Physics*, 2007, **102**, 073512.

[32]   B. F. Monzyk, E. C. Burckle, L. M. Carleton, J. Busch, K. A. Dasse, P. M. Martin and R. J. Gilbert, *ASAIO Journal*, 2006, **52**, 456-466.

[33]   A. Subrahmanyam, T. Arokiadoss and T. P. Ramesh, *Artificial Organs*, 2007, **31**, 819-825.

[34]   A. Subrahmanyam, T. P. Ramesh and N. Ramakrishnan, *ASAIO Journal*, 2007, **53**, 434-437.

[35]   W.S. Kuo and P.H. Ho, *Chemosphere*, 2001, **45**, 77-83.

[36]   M. Panizza, A. Barbucci, R. Ricotti and G. Cerisola. *Separation and. Purification. Technology*, 2007, **54**, 382-387.

[37]   S. Lakshmi, R. Renganathan and S. Fujita. *Journal of Photochemistry and Photobiology A*, 1995, **88**, 163-167.

[38]   A. Houas, H. Lachheb, M. Ksibi, E. Elaloui, C. Guillard and J.M. Herrmann, *Applied Catalysis B*, 2001, **31**, 145–157.

[39]   P. G. Hattersley, *Journal of the America Medical Association*, 1966, **196**, 436-440.